SYSTEMS, SCIENCE AND SOFTWARE

SSS-R-77-3038

IMPROVED YIELD DETERMINATION AND EVENT IDENTIFICATION RESEARCH

J. M. Savino
T. C. Bache
T. G. Barker
J. T. Cherry
D. G. Lambert
J. F. Masso
N. Rimer
W. O. Wray

Final Report

For Period May 1, 1975 - September 30, 1976

D D C
RECEIVED
NOV 21 1977
B

The views and conclusions contained in this document are those of the authors and should not be interpreted as necessarily representing the official policies, either expressed or implied, of the Advanced Research Projects Agency, the Air Force Technical Applications Center, or the U.S. Government.

October 1976

P. O. BOX 1620, LA JOLLA, CALIFORNIA 92038, TELEPHONE (714) 453-0060

SYSTEMS, SCIENCE AND SOFTWARE

SSS-R-77-3038

IMPROVED YIELD DETERMINATION AND EVENT IDENTIFICATION RESEARCH

J. M. Savino
T. C. Bache
T. G. Barker
J. T. Cherry
D. G. Lambert
J. F. Masso
N. Rimer
W. O. Wray

Final Report

For Period May 1, 1975 - September 30, 1976

The views and conclusions contained in this docu-
ment are those of the authors and should not be
interpreted as necessarily representing the of-
ficial policies, either expressed or implied, of
the Advanced Research Projects Agency, the Air
Force Technical Applications Center, or the U.S.
Government.

Approved for Public Release, Distribution Unlimited

October 1976

SECURITY CLASSIFICATION OF THIS PAGE *(When Data Entered)*

REPORT DOCUMENTATION PAGE		READ INSTRUCTIONS BEFORE COMPLETING FORM
1. REPORT NUMBER	2. GOVT ACCESSION NO.	3. RECIPIENT'S CATALOG NUMBER
4. TITLE *(and Subtitle)* IMPROVED YIELD DETERMINATION AND EVENT IDENTIFICATION RESEARCH.		5. TYPE OF REPORT & PERIOD COVERED Final – May 1, 1975 – Sept. 30, 1976
		6. PERFORMING ORG. REPORT NUMBER SSS-R-77-3038
7. AUTHOR(s) J. M. Savino, T. C. Bache, T. G. Barker, J. T. Cherry, D. G. Lambert, J. F. Masso, N. Rimer and W. O. Wray		8. CONTRACT OR GRANT NUMBER(s) Contract No. F08606-75-C-0045
9. PERFORMING ORGANIZATION NAME AND ADDRESS Systems, Science and Software P. O. Box 1620 La Jolla, CA 92038		10. PROGRAM ELEMENT, PROJECT, TASK AREA & WORK UNIT NUMBERS Program Code No. 6F10 ARPA Order No. 2551
11. CONTROLLING OFFICE NAME AND ADDRESS VELA Seismological Center 312 Montgomery Street Alexandria, VA 22314		12. REPORT DATE October 1976 13. NUMBER OF PAGES 70p.
14. MONITORING AGENCY NAME & ADDRESS*(if different from Controlling Office)* Final rept. 1 May 75 – 30 Sep 76,		15. SECURITY CLASS. *(of this report)* UNCLASSIFIED
		15a. DECLASSIFICATION/DOWNGRADING SCHEDULE

16. DISTRIBUTION STATEMENT *(of this Report)*

Approved for Public Release, Distribution Unlimited

17. DISTRIBUTION STATEMENT *(of the abstract entered in Block 20, if different from Report)*

18. SUPPLEMENTARY NOTES

Work performed on this contract has been reported in a series of 11 topical and

19. KEY WORDS *(Continue on reverse side if necessary and identify by block number)*

Explosion Seismology
Explosion Source Functions
Multiple Explosions
Constitutive Models

Yield Estimation Techniques
Seismic Ground Motion
Teleseismic Magnitudes

20. ABSTRACT *(Continue on reverse side if necessary and identify by block number)*

Work performed on Contract No. F8606-75-C-0045 has been reported in detail in a series of eleven topical and quarterly technical reports. This final report summarizes the material covered in each of the technical reports and discusses the conclusions obtained. The primary objective of the program is to develop methods for estimating the yield of underground nuclear explosions. The topics addressed include the modeling of both single and multiple explosions, propagation of the resultant stress waves through realistic earth

(cont on p ii)

DD FORM 1473 EDITION OF 1 NOV 65 IS OBSOLETE
1 JAN 73

388 507 i

(cont'd pi)

structures, and prediction of short- and long-period explosion seismograms recorded at teleseismically located receivers. The results of these investigations provide a theoretical framework for expressing uncertainties in explosion yield estimates in terms of uncertainties in the near source material properties, local source and receiver crustal structures, and the upper mantle structure of the earth.

A

TABLE OF CONTENTS

LIST OF FIGURES

LIST OF TABLES

I.   SUMMARY

Work performed on Contract No. F8606-75-C-0045 has been reported in detail in a series of eleven topical and quarterly technical reports. This final report summarizes the material covered in each of the technical reports and discusses the conclusions obtained. The primary objective of the program is to develop methods for estimating the yield of underground nuclear explosions. The topics addressed include the modeling of both single and multiple explosions, propagation of the resultant stress waves through realistic earth structures, and prediction of short- and long-period explosion seismograms recorded at teleseismically located receivers. The results of these investigations provide a theoretical framework for expressing uncertainties in explosion yield estimates in terms of uncertainties in the near source material properties, local source and receiver crustal structures, and the upper mantle structure of the earth.

II.   INTRODUCTION

This final report summarizes work performed under
Contract Number F8606-75-C-0045, entitled, "Improved Yield
Determination and Event Identification Research", by
Systems, Science and Software (S³) in La Jolla, California.
The program, which was conducted during the period from 1
May 1975 through 30 September 1976, consisted of the follow-
ing major tasks:

- A combined theoretical/empirical evaluation of
  the effects of variations in near source material
  properties and emplacement parameters on explo-
  sion generated body and surface waves used for
  establishing magnitude-yield relationships.

- Development of procedures for predicting tele-
  seismic signals from explosions and estimating
  uncertainties in seismically determined yields
  in terms of uncertainties in gross earth struc-
  ture, and local source and receiver structure.

Detailed results obtained for these tasks have been
presented in a series of Technical Reports. These results
are summarized in the following section of this final re-
port. All reports prepared under this contract are listed
in the Appendix.

III. SUMMARY OF TECHNICAL RESULTS

3.1   TECHNICAL REPORT NO. 1

"Seismic Coupling from a Nuclear Explosion: The Dependence of the Reduced Displacement Potential on the Nonlinear Behavior of the Near Source Rock Environment," Cherry, et al., September, 1975.

3.1.1 Introduction

This report describes the results of a theoretical study directed at the determination of the sensitivity of the equivalent elastic source from a nuclear explosion to the nonlinear behavior of the near source rock environment. The results of the parameter study provide valuable insight concerning the importance of various material parameters for accurate prediction of seismic coupling. The results also aid in the establishment of guidelines for the collection of geophysical data in the near source region.

3.1.2 Theoretical Considerations

A relationship between the teleseismically determined body wave magnitude, m_b, and the elastic properties of the near source material is given as

$$m_b \sim \log \left[\alpha \, \Psi(\infty) \right] \tag{3.1}$$

where $\Psi(\infty)$ is the steady state value of the reduced displacement potential and α is the near source compressional wave speed. This relationship was derived by considering the impedence contrast between the low velocity source region and the basement rock. Not included in this relationship are the effects of pP or any of the details of the geophysical properties of the crustal layers.

3

If $\Psi_i(\infty)$ and $\Psi_k(\infty)$ are two values of $\Psi(\infty)$ corresponding to materials i and k, then the change in teleseismic magnitude is given by

$$\Delta m = m^i - m^k = \log\left[\frac{\alpha_i \, \Psi_i(\infty)}{\alpha_k \, \Psi_k(\infty)}\right] . \qquad (3.2)$$

Equation (3.2) gives the scaling law for teleseismic magnitudes in terms of $\alpha \, \Psi(\infty)$. This equation is always valid as long as the spectrum of the equivalent source is flat within the teleseismic frequency band and path effects associated with earth structure are invariant between events. Finally, uncertainties in yield estimates based on experimentally determined seismic magnitudes may be related to uncertainties in near source material properties via direct application of Eq. (3.2).

3.1.3 Results of Parameter Study

The results of the sensitivity study are summarized in Table 3.1. Some general remarks are in order before discussing the effect of individual parameter variations. Note that the ambient density, ρ_0, and the bulk modulus, k_0, are included in the table although they are not independent parameters in the context of this study; i.e., their values are determined by the independent parameters appearing in the first ten columns. Calculation No. 18 is selected as the reference for body and surface wave magnitude variations in order to avoid the appearance of minus signs in the Δm_b column. Calculations marked with an asterisk in the $\Psi(\infty)$ column were performed with a new source description which gave an RDP 42 percent higher than the RDP obtained in Calculation No. 8 using the old source description; the RDP's calculated with the new source description were therefore scaled down by a factor of 0.704 and the scaled values are

4

TABLE 3.1

RESULTS OF PARAMETER SENSITIVITY STUDY

f_w	ϕ_0	P_e (kbar)	P_c (kbar)	α (km/sec)	μ (kbar)	Y_0 (kbar)	Y_{MAX} (kbar)	P_m (kbar)	P_0 (kbar)	ρ_0 (gm/cm³)	k_0 (kbar)	$Y(\infty)$ (m³)	Δm_b	Calculation Number
0	0	—	—	3.87	40.0	0	0.5	0.6	0.216	2.4	294.4	13.88	1.2862	1
0.05	0	—	—	2.80	40.0	0	0.5	0.6	0.116	2.243	121.8	10.01	1.0104	2
0.136	0	—	—	2.44	40.0	0	0.5	0.6	0.116	2.015	66.5	7.85	0.8451	3
0.17	0	—	—	2.40	40.0	0	0.5	0.6	0.116	1.938	57.8	7.34	0.8088	4
0.19	0	—	—	2.38	40.0	0	0.5	0.6	0.116	1.895	53.8	7.09	0.7901	5
0.17	0.02	0.075	0.5	2.40	40.0	0	0.5	0.6	0.116	1.90	56.1	3.60	0.4994	6
0.17	0.05	0.075	0.5	2.40	40.0	0	0.5	0.6	0.116	1.84	52.6	2.10	0.2653	7
0.17	0.05	0.075	0.5	2.40	40.0	0	1.0	0.6	0.116	1.84	52.6	1.35	0.0734	8
0.17	0.05	0.15	0.5	2.40	40.0	0	1.0	0.6	0.116	1.84	52.6	1.48*	0.1133	9
0.17	0.02	0.075	0.5	2.40	40.0	0	0.5	0.6	0.075	1.90	56.1	4.20	0.5663	10
0.17	0.02	0.075	1.25	2.40	40.0	0	0.5	0.6	0.075	1.90	56.1	4.60	0.6059	11
0.17	0.05	0.075	0.5	2.32	40.0	0	1.0	0.6	0.116	1.84	45.7	1.31*	0.0456	12
0.17	0.05	0.075	0.5	2.25	40.0	0	1.0	0.6	0.116	1.84	39.8	1.29*	0.0257	13
0.17	0.05	0.075	0.5	2.40	42.0	0	1.0	0.6	0.116	1.84	50.0	1.28*	0.0503	14
0.17	0.05	0.075	0.5	2.40	45.0	0	1.0	0.6	0.116	1.84	46.0	1.17*	0.0113	15
0.17	0.05	0.075	0.5	2.40	40.0	0.1	1.0	0.6	0.116	1.84	52.6	1.32*	0.0637	16
0.17	0.05	0.075	0.5	2.40	40.0	0.2	1.0	0.6	0.116	1.84	52.6	1.31*	0.0604	17
0.17	0.05	0.075	0.5	2.40	40.0	1.0	1.0	0.6	0.116	1.84	52.6	1.14*	0	18
0.17	0.02	0.075	0.5	2.40	40.0	0	0.5	1.25	0.075	1.90	56.1	7.70	0.8296	19
0.17	0.02	0.075	0.5	2.40	40.0	0	0.5	0.6	0.348	1.90	56.1	2.41	0.3251	20
0.17	0.02	0.075	0.5	2.40	40.0	0	0.5	0.6	0.619	1.90	56.1	2.08	0.2612	21
0.17	0.05	0.075	0.5	2.40	40.0	0	0.75	0.6	0.116	1.84	52.6	1.51*	0.1221	22

*Calculation performed with new source description.

reported in Table 3.1. All calculations appearing in Table 3.1 were performed with a device yield of 20 tons.

Since the elastic properties of the near source material appear in the magnitude relation, Eq. (3.2), via the P wave velocity, α, it is obviously important to determine their values accurately. As can be seen from Table 3.1, a positive error in determination of α would cause body wave magnitude to be over-predicted.

The steady state value of the RDP, $\Psi(\infty)$, which appears in the magnitude relation, Eq. (3.2), is dependent on the shock response of the near source material. Referring to Table 3.1, the near source material properties which have the most pronounced effect on the shock response are the water mass fraction, f_w, and the air-filled void fraction, ϕ_0. Positive errors in either f_w or ϕ_0 could lead to substantial under-prediction of seismic magnitudes. The variation of seismic magnitude as a function of ϕ_0 is presented in Figure 3.1. Note that the introduction of air-filled voids causes a drastic reduction in seismic coupling and the importance of establishing this parameter preshot is obvious.

Seismic magnitude is not very sensitive to P_e, the elastic pressure, and P_c, the crush pressure, indicating that details in the porosity model are relatively unimportant.

Seismic magnitudes are, however, very sensitive to the parameters which describe the failure surface. If Y_0, Y_m, or P_m are varied such that the material strength is enhanced the coupling efficiency of an explosive device is impaired. Thus, a positive error in the material strength would lead to an under-prediction of seismic magnitude.

6
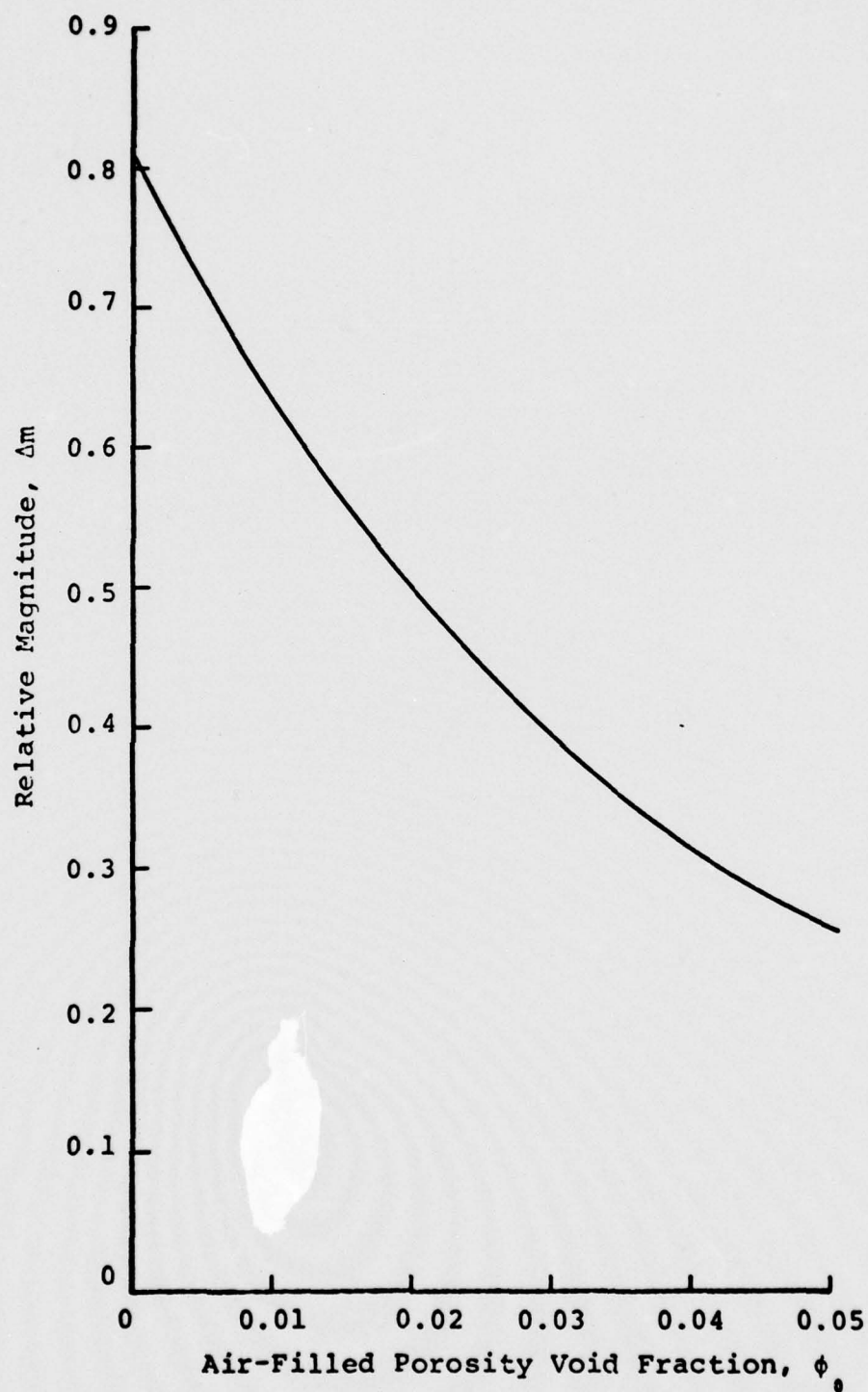
Figure 3.1. Effect of air-filled porosity on seismic magnitude.

3.2   TECHNICAL REPORT NO. 2

"Teleseismic Coupling from the Simultaneous Detonation of an Array of Nuclear Explosions," Cherry, et al., February, 1976.

3.2.1 Introduction

The problem addressed in this report involves the calculation of teleseismic ground motion produced by three 15 kt nuclear sources detonated simultaneously. The three sources were equally spaced 165 meters apart and were assumed to be contained, i.e., coupling effects due to cratering were not included in the analysis.

In an earlier series of calculations reported by Cherry, et al., (1975b), the region of tension failure resulting from the shock interaction of the three explosions engulfed most of the calculational grid, allowing only for qualitative estimates of the effects on seismic coupling. An improved grid was used for subsequent calculations described in Report No. 2. The discussion that follows is based on results from Report No. 2.

3.2.2 Near Source Ground Motion

The techniques used to predict the teleseismic ground motion from our explosive array require that the divergence, $\nabla \cdot \vec{S}$, and curl, $\nabla \times \vec{S}$, of the displacement field be monitored over a spherical surface which is outside the nonlinear material response region. The time histories of $\nabla \cdot \vec{S}$ and $\nabla \times \vec{S}$ are then decomposed into a multiple expansion in spherical harmonics. This expansion provides an equivalent point source representation which may be used to quantitatively establish the seismic coupling of the array.

Figure 3.2 shows a sketch of the explosive array, the nonlinear region and the spherical surface over which $\nabla \cdot \vec{S}$ and $\nabla \times \vec{S}$ were monitored. The computational grid extended far enough beyond this surface so that external reflections would not obviate the free field assumption.

The tensile fracture pattern around two adjacent cavities 6.85 msec after detonation is shown in Figure 3.3. Note the "pre-splitting" between the cavities and the alteration of the fracture pattern from that expected from a spherically symmetric explosive source. This last item is illustrated dramatically in Figure 3.4 which shows the distribution of fractures in the entire grid at 11.57 msec. The fracture pattern above and to the left of the outer source is that expected from a single explosive. The alteration of this fracture pattern is caused by interaction of the stress fields from adjacent explosives.

3.2.3 Teleseismic Ground Motion

In order to study the far field seismic signature of an explosive event like that considered here, it is necessary to merge the nonlinear finite difference source calculations presented in the previous subsection of this report with the elastic wave propagation methods of theoretical seismology. This is done via an equivalent elastic source representation of the multiple explosion source.

The familiar reduced displacement potential, RDP, representation of a spherically symmetric explosion is an elementary equivalent elastic source. For more complex sources a representation in terms of an expansion of the outgoing displacement field in spherical harmonics is appropriate. The calculation of an equivalent elastic source in this latter form for a complex asymmetric explosion source was first accomplished by Cherry, et al. [1975a]. A detailed

Spherical surface over
which the divergence
and curl of the dis-
placement field were
monitored.

Elastic Region

450 m

← 165 m → ← 165 m →

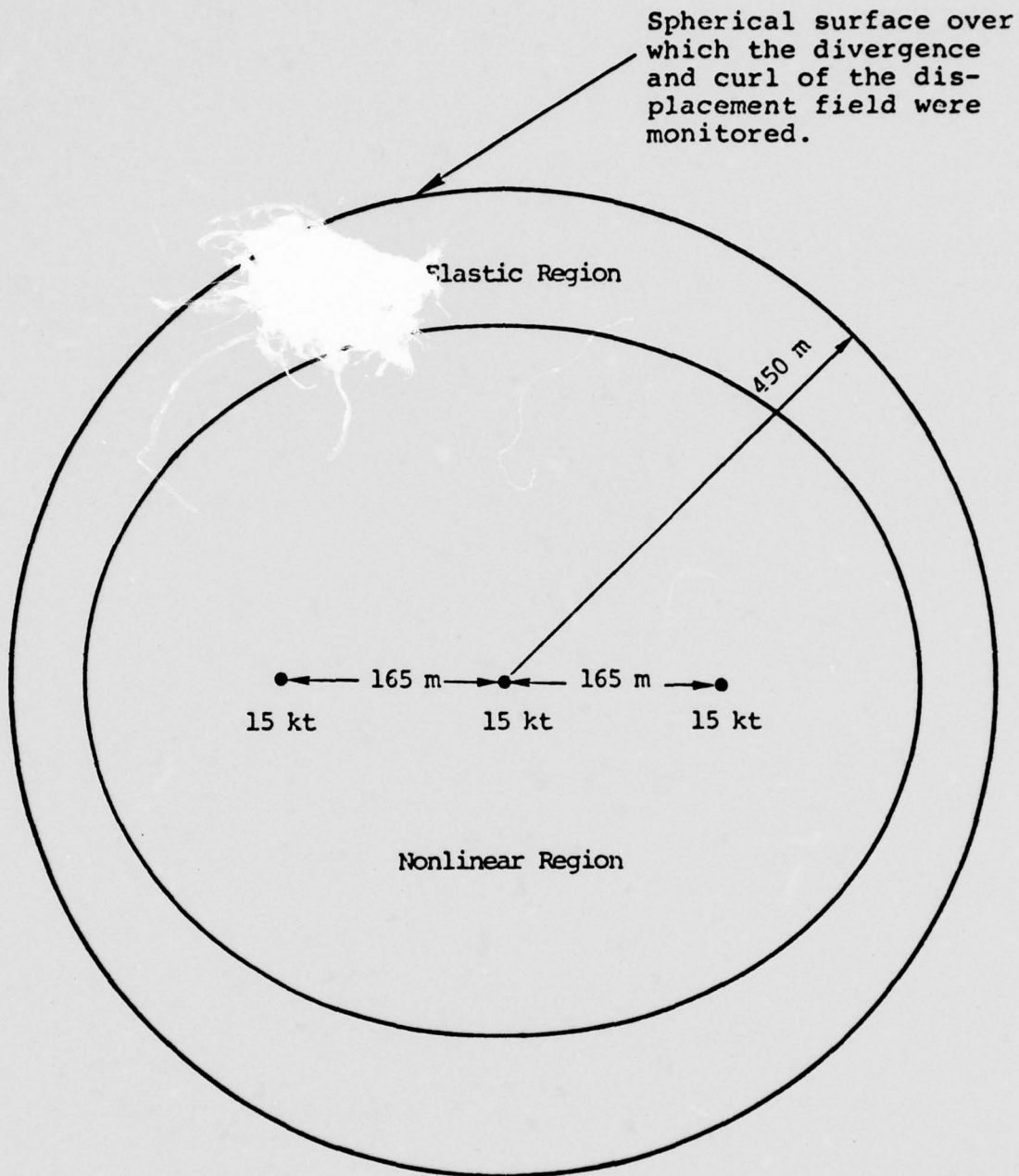15 kt   15 kt   15 kt

Nonlinear Region

Figure 3.2.   Sketch of the explosive array, the resulting
nonlinear region and the surface over which
the properties of the outgoing displacement
field were monitored.
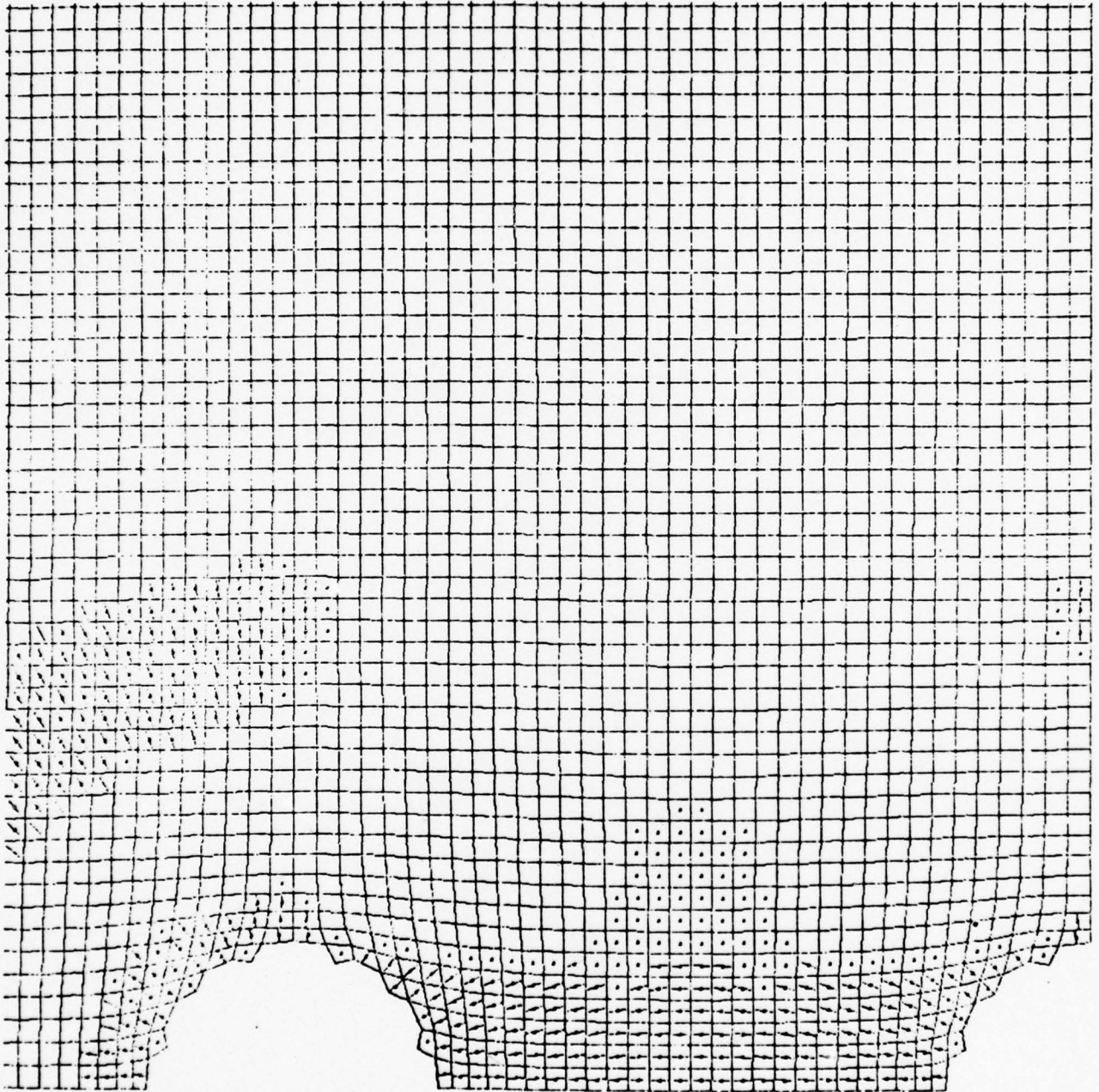
Figure 3.3. Crack location and orientation 6.85 msec after detonation.
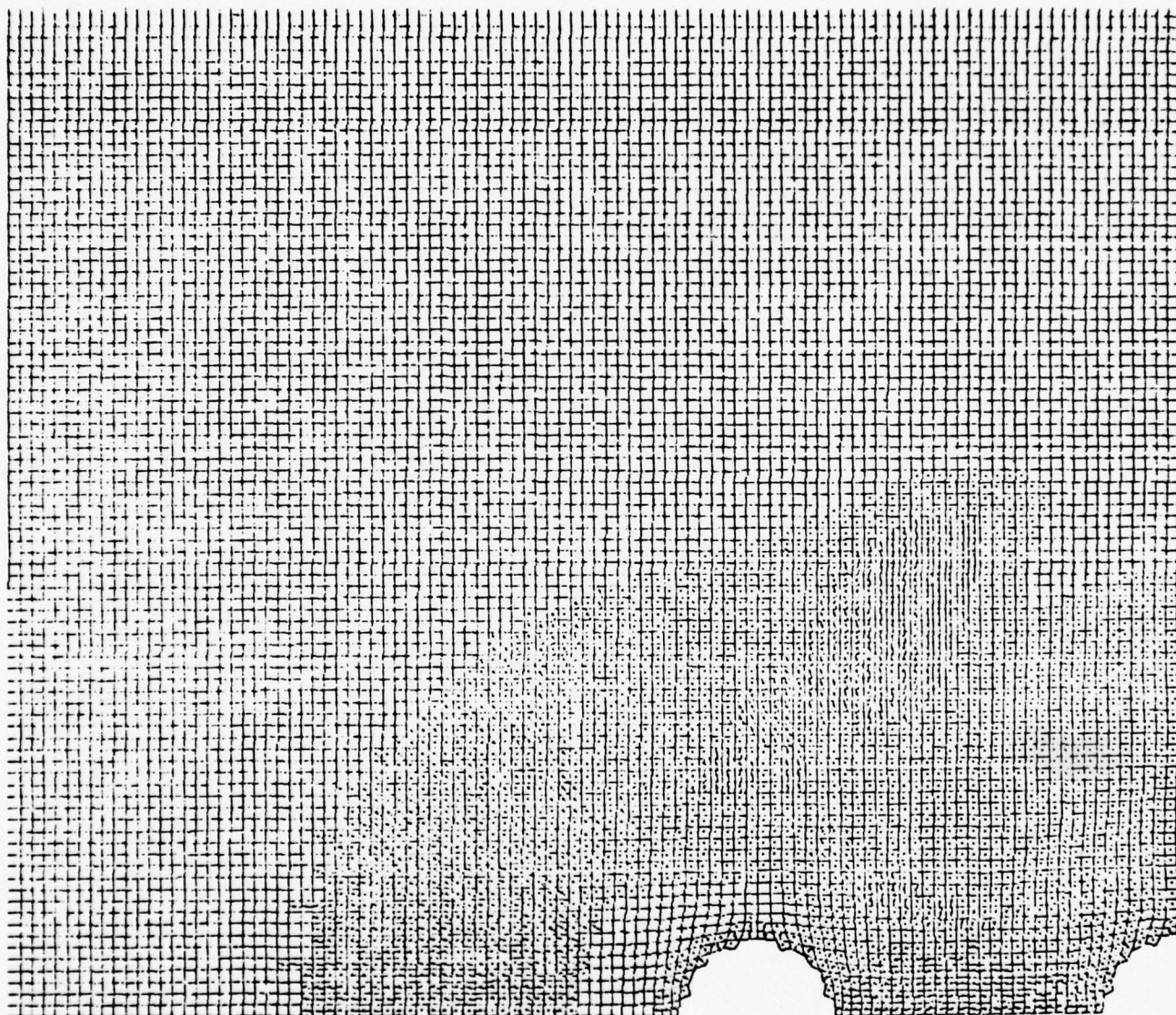
Figure 3.4. Complete crack location and orientation 11.57
msec after detonation.

presentation of the theory and its implementation is given by Bache, et al. [1975a].

In Figure 3.5 the amplitude of the transformed reduced velocity potential, $|\hat{\Psi}(\omega)|$, from the 1-D calculations is compared to the equivalent quantity for the two multiple explosions under study. The linear superposition is done by (1) scaling the source as if it were a single 45 kt explosion and (2) considering the event to be the superposition of three 15 kt explosions. Due to the cube root scaling laws, the only difference in the two is that the second representation is somewhat richer in high frequencies.

From Figure 3.5, we see that the "equivalent RDP" from the spherically symmetric portion of the multiple explosion calculation does not differ substantially from that obtained by a linear superposition of one-dimensional sources. It is interesting to note that the corner frequency for the no tensile failure calculation falls between that for the 3 × 15 kt and 45 kt superposition sources. For the second calculation, with tensile failure, the "equivalent RDP" is very little different than that for the 45 kt source.

3.2.4 Conclusions

Calculations performed to date have produced no significant enhancement of teleseismic ground motion from a multiple shot array. This was true in spite of the fact that the near source fracture pattern from the array differed significantly from that produced by a spherically symmetric explosion source. Fairly large perturbations in the seismic radiation pattern did appear but at frequencies outside the teleseismic band.

Enhanced tension failure did occur in the multiple shot calculation. However, for this to seriously affect teleseismic ground motion it would require an explosive
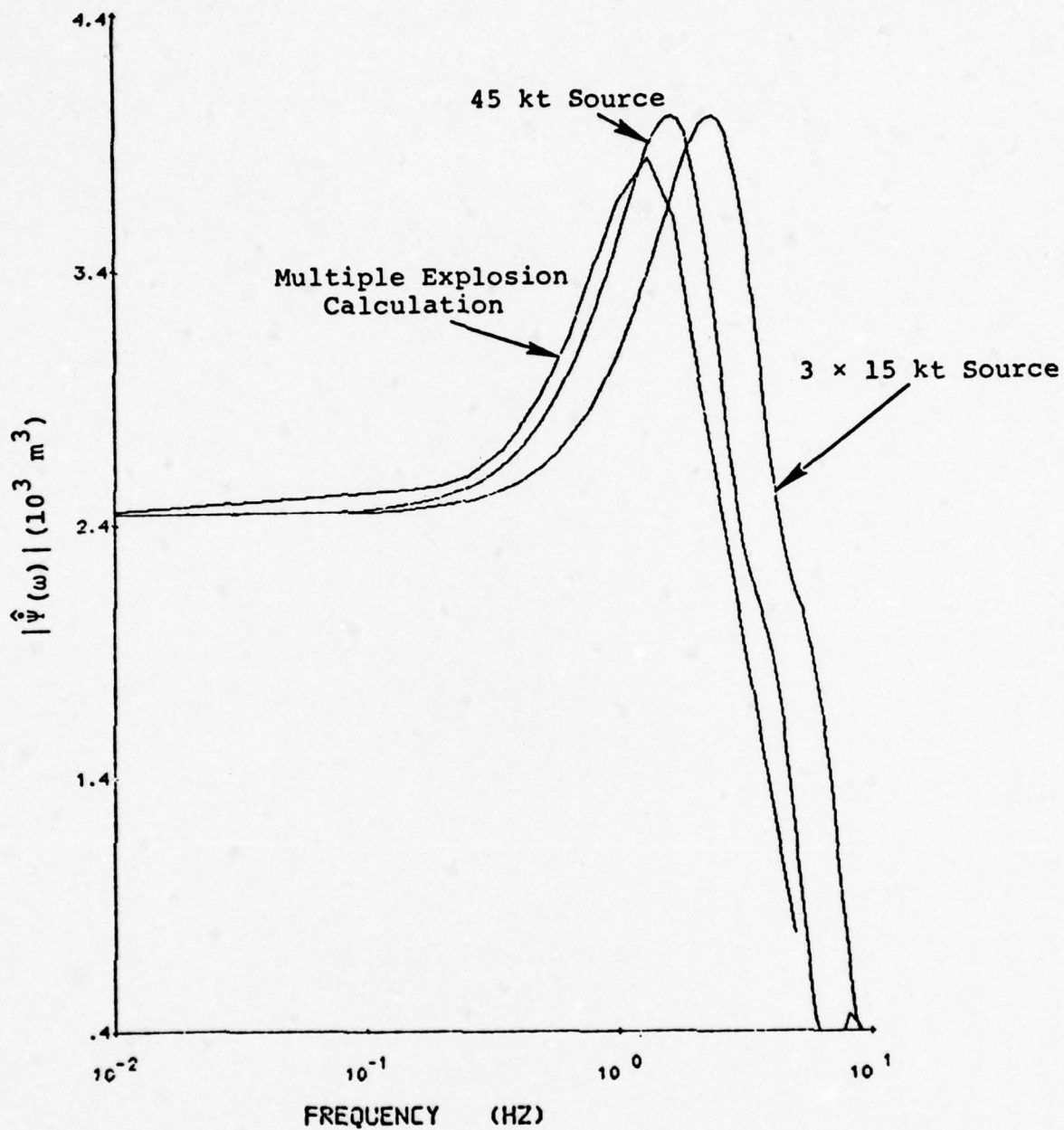
Figure 3.5. Comparison of the "equivalent RDP" representations of the multiple explosion for the calculations including the effect of tensile failure.

14

spacing, yield and material properties combination in which fracturing from the array is much greater than that produced by a single charge of equivalent yield.

An array in which the important parameters are optimized to significantly alter the teleseismic ground motion could probably be constructed. However, it is much more likely that anomalous observations of teleseismic ground motion from an explosive array are due to overburden effects and high (low) coupling material properties. If these factors fail to explain the anomaly, shock interaction calculations should be performed but should be based on a good estimate of material strength for the rock at the test site.

3.3 TECHNICAL REPORT NO. 3

"Constitutive Equations for Fluid-Saturated Porous Media", Garg, S. K., October, 1975.

3.3.1 Introduction

This report describes the development of constitutive relations for fluid-saturated porous media, suitable for inclusion in standard hydrodynamic codes (e.g., CRAM or SKIPPER). The theoretical formulation is based on models for fluid-saturated rock aggregates previously developed by Garg and Nur [1973] and Garg, et al. [1975].

In the development of the constitutive model it is assumed that (1) there is no relative motion between the fluid and the solid, (2) no significant heat exchange occurs between the solid and fluid phases, and (3) porosity ϕ is a function of only the mixture pressure P_c and the fluid pressure P_f. The last two assumptions may not be valid under certain field conditions and can be relaxed, although at the expense of some simplicity.

15

The first assumption (no fluid diffusion) is equivalent to requiring [Garg, et al., 1975] that

$$X >> \frac{C_0 \, k \, p_0}{\phi^2 \, \mu_f} \quad ,$$

where

$X \sim$ length scale of interest,

$\mu_f \sim$ fluid viscosity,

$p_0 \sim$ density of porous media,

$C_0 \sim$ speed of sound in porous media,

$k \sim$ permeability of porous media, and

$\phi \sim$ porosity.

It is straightforward to verify that the above inequality is satisfied for many field situations involving shock/seismic wave propagation in fluid-saturated porous media. This report concludes with an iterative procedure for incorporating this new constitutive model into standard hydrodynamic codes.

3.4 TECHNICAL REPORT NO. 4 AND TECHNICAL REPORT NO. 5

"Prediction and Matching of Teleseismic Ground Motion (Body and Surface Waves) From the NTS MAST Explosion," Barker, et al., February, 1976.

"Comparison of Theoretical and Observed Body and Surface Waves for KASSERI, an Explosion at NTS," Bache, et al., May, 1976.

3.4.1 Introduction

These reports present the results of a theoretical calculation of the teleseismic body and surface waves for the underground explosion MAST and KASSERI, and a detailed

comparison of the synthetic seismograms recorded at the stations of the Special Data Collection System (SDCS). This study is a comprehensive analysis of both explosions using computer modeling of the close-in nonlinear ground motion produced by each explosion, propagation of the resulting seismic waves through realistic earth structures and computation of synthetic seismograms at designated teleseismic stations. One of the important questions addressed by this exercise is: What pre-shot measurements of the near-source medium are required in order to predict the amplitude of the seismic signal to within some specified range?

3.4.2 Explosion Source Functions

Fundamental to the prediction of teleseismic ground motion from explosions is the calculation of the explosion reduced displacement potential (RDP) which represents the source coupling into elastic waves. The coupling was computed using the one-dimensional (spherically symmetric) finite difference code, SKIPPER.

A series of source calculations were made for KASSERI and MAST. The KASSERI explosion was detonated in ash flow tuff at Area 20, Pahute Mesa. The working point was well below the water table. Standard measurements for density, grain density, overburden density, water content, saturation and P wave velocity were available.

No material strength data were available for KASSERI. Therefore, we were forced to estimate the material strength from other information. A parameter study of the effect of plausible strength variations on the seismic signal was carried out as part of the KASSERI investigation.

The amplitude of the reduced velocity potential, $|\dot{\Psi}(\omega)|$, is plotted in Figure 3.6 for four (146-149) KASSERI
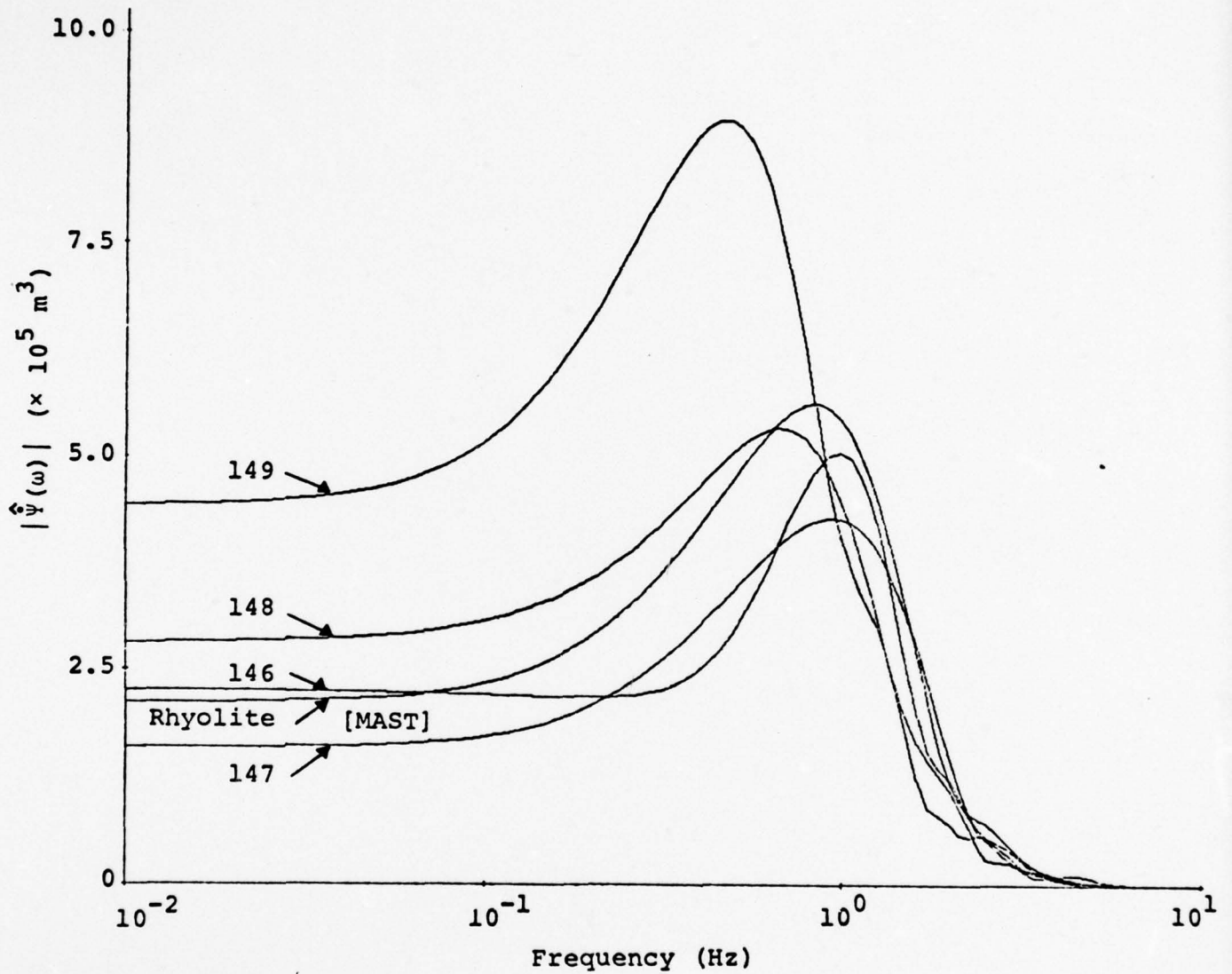
Figure 3.6. The source function amplitudes for the tuff
sources of Table 3.1 and the rhyolite source
used for MAST. The source functions are all
scaled to 1000 kt.

18

sources and the rhyolite source used for MAST. The $\hat{\Psi}(\omega)$ is essentially the far field displacement spectrum. In fact,

$$m_b \approx \log \alpha \, \hat{\Psi} \, (1 \text{ Hz}),$$

$$M_s \approx \log \mu \, \hat{\Psi} \, (0.05 \text{ Hz}),$$

as has been demonstrated theoretically in a number of past S^3 reports [e.g., Bache, et al., 1975a, 1975b].

Comparing calculations 146 and 147, we see that the low strength portion of the strength curve significantly narrows the peaked portion of the spectrum while having a relatively minor effect elsewhere. Comparing 147, 148 and 149, as the strength is decreased the spectrum gets larger. Also, the peak becomes narrower and moves to lower frequencies. The MAST source exhibits behavior between that of 147 and 148.

For MAST and KASSERI the important parameters controlling the teleseismic coupling are $\alpha = 4.2$ km/sec, $\mu = 169$ kbar for MAST and $\alpha = 3.1$ km/sec and $\mu = 90$ kbar for KASSERI. These values together with the source functions in Figure 3.6 give a first estimate of the relative size of the body and surface waves for these two events. Detailed comparison of theoretical and observed seismograms is made in the following section.

3.4.3 Teleseismic Body Wave Predictions for KASSERI and MAST

The teleseismic body wave comparisons are shown in Figure 3.7. For each of the five SDCS stations at which theoretical seismograms were made, we show first the comparison of predicted and observed seismograms for MAST and then for KASSERI. The important result is that the agreement at each of the individual stations is well within a factor of two in amplitude.
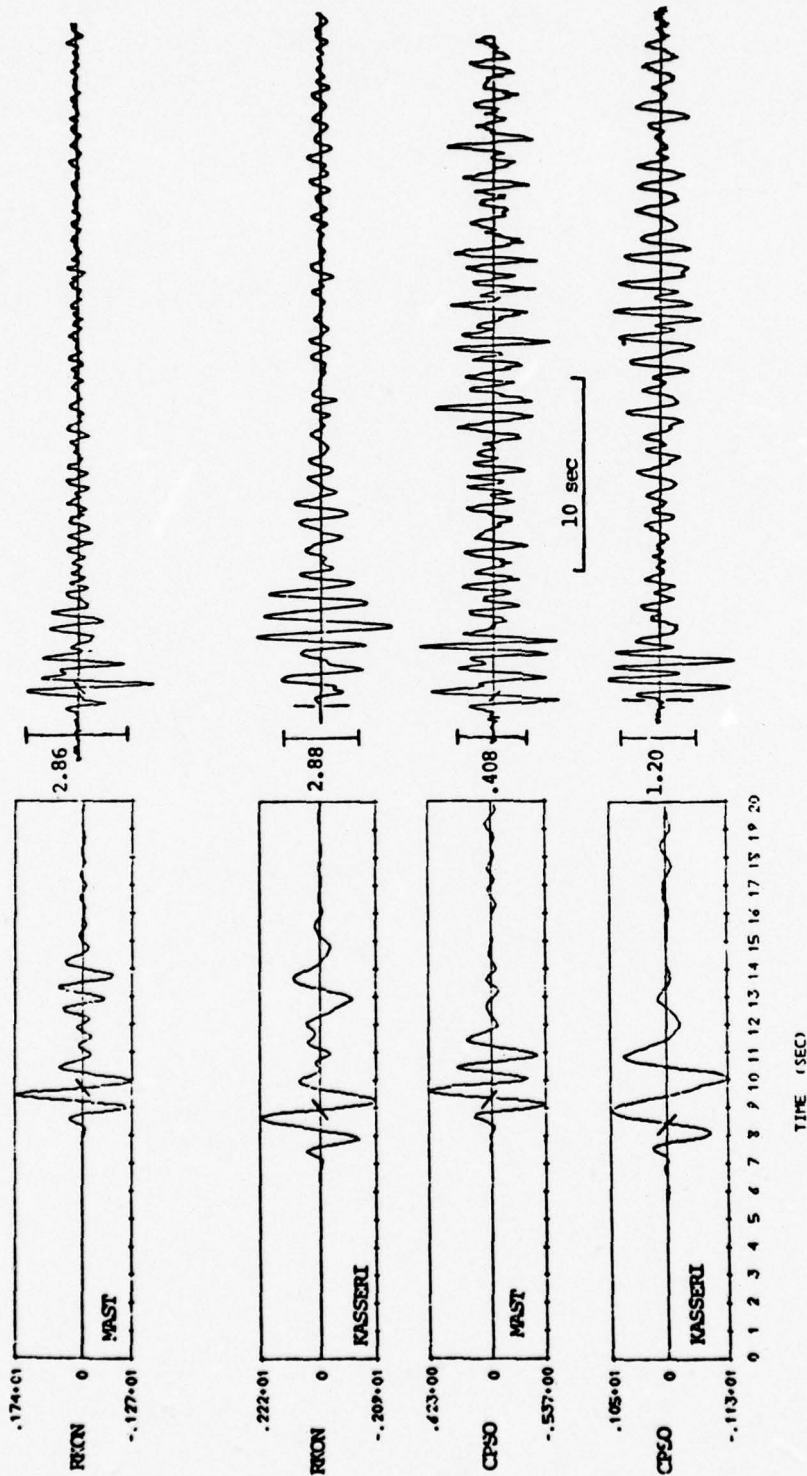
19

Figure 3.7. Comparison of synthetic (left) and observed short period vertical component seismograms at five SDCS stations for the events MAST and KASSERI. The amplitude at 1 Hz is indicated at the left on each record. The bars show the cycle at which the maximum of "d" amplitude measurements were made.
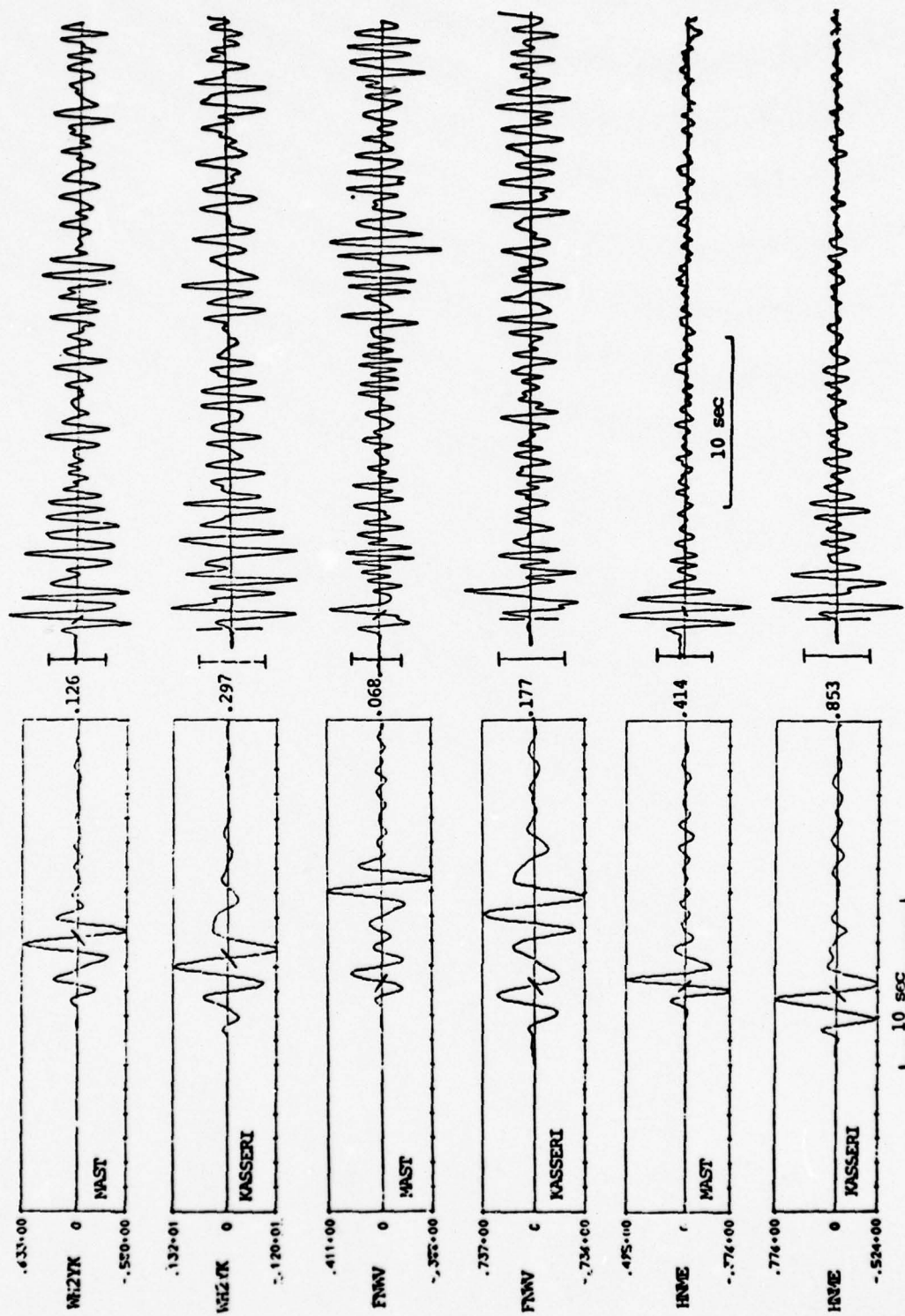
20

Figure 3.7. (Continued)

21

The source crustal structures over the top two kilo-
meters were taken from the respective Containment Evaluation
Panel (CEP) reports. At greater depths the structures were
taken to be the same. For the structure at the receiver an
average crustal model having little effect on the seismo-
grams was used at all the SDCS stations. For the upper
mantle we chose a slightly modified version of the Helmberger
and Wiggins [1971] model HWNE.

The comparison between theoretical and observed ampli-
tudes from the seismograms of Figure 3.7 is shown in Figures
3.8 and 3.9. The data in Figure 3.8 are for the "b" phase;
those in Figure 3.9 are for the maximum amplitude in the
first three cycles, the "d" phase. Along with the plotted
b and d amplitudes, the periods of the cycles at which these
measurements were made also appear on the figures.

From the comparison of Figures 3.8 and 3.9, we can
draw the following conclusions:

● The scaling of observed amplitudes between the
   two events is quite consistent except for RKON.
   We previously pointed out the marked dissimilarity
   in waveforms at RKON for these two events.

● The match between theoretical and observed ampli-
   tudes is about the same for the two events. The
   exceptional stations are RKON and FNWV. It will
   be very difficult to explain the RKON anomaly
   with present techniques since the epicentral
   distance variation between events is only 0.1
   degrees. Waveform similarities at WH2YK, CPSO
   and HNME discourage attempts to attribute the
   anomaly to near source effects. Even in our
   theoretical model the interference pattern at
   FNWV is enough to make the b amplitude behave
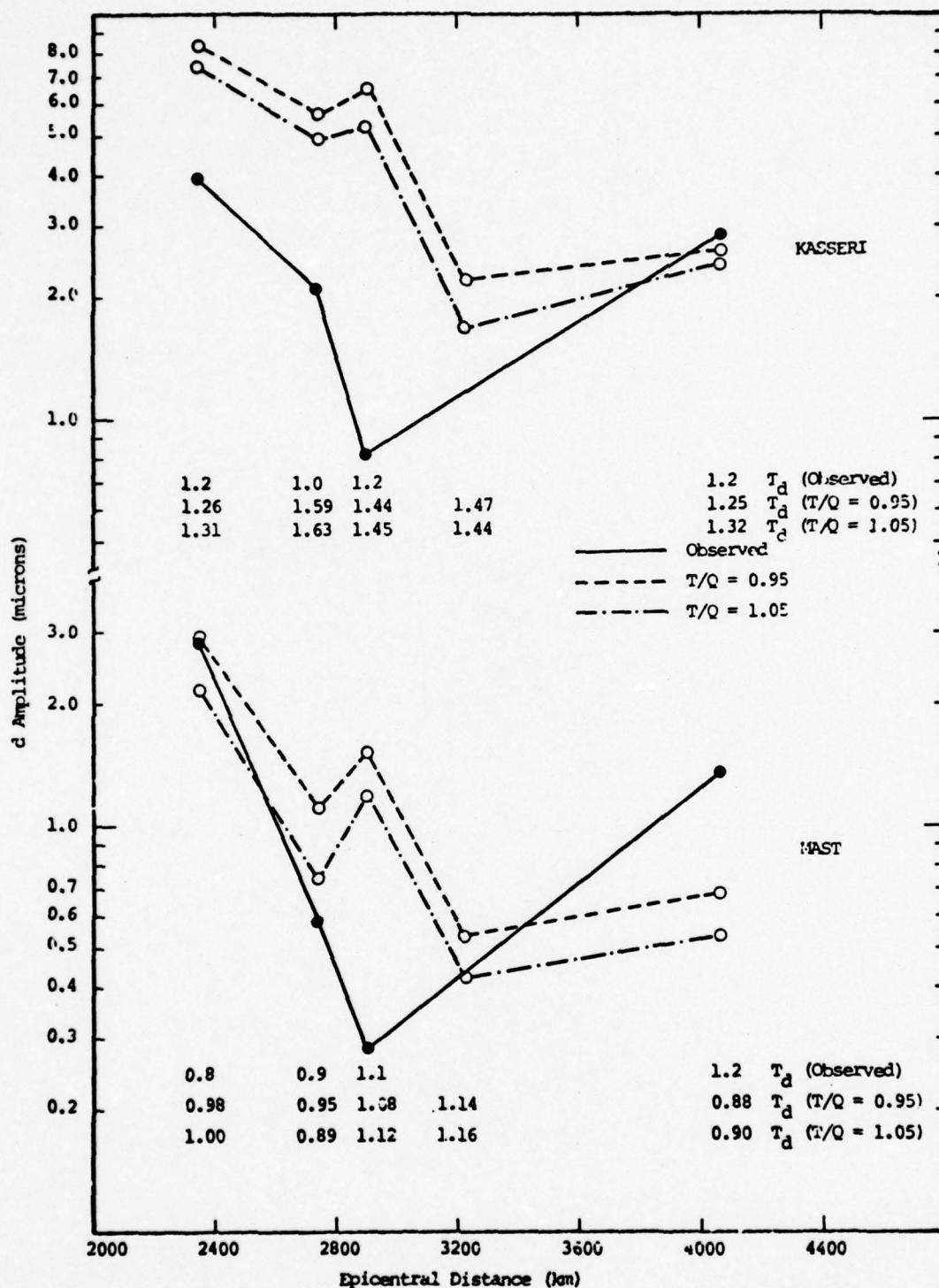   erratically as we see by comparing results for

22

Figure 3.8.   Comparison of theoretical and observed b ampli-
tudes for MAST and KASSERI at five SDCS stations.
Seismograms were computed for two values of T/Q
as indicated. The KASSERI source function is
denoted 148 and the upper mantle model is HWNE-3.
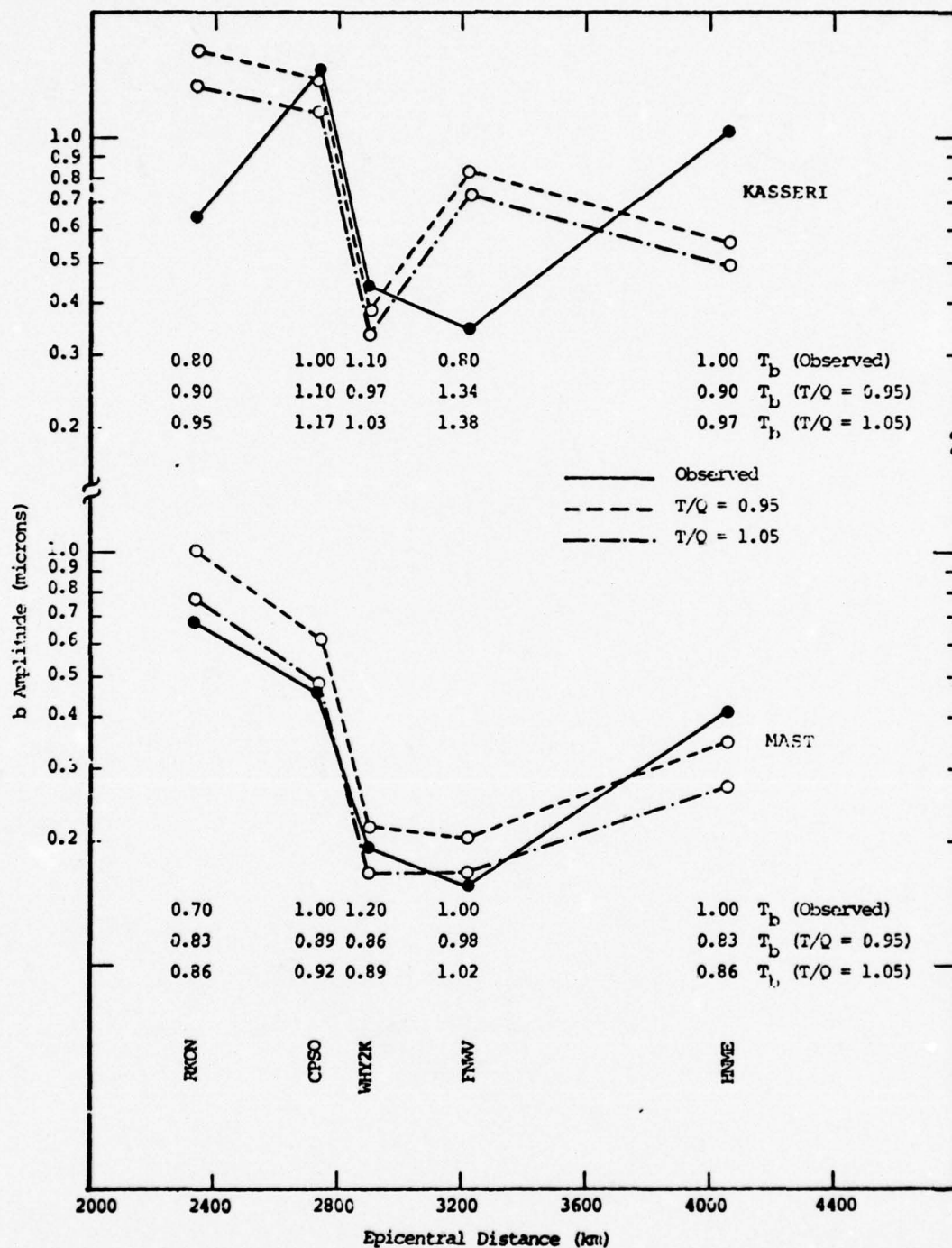
Figure 3.9. Comparison of theoretical and observed d amplitudes for MAST and KASSERI.

the two events. However, it is unlikely that
current modeling techniques, no matter how ac-
curately used, would permit a very accurate
duplication of observed records at this station.

● The scaling between the two computed source
functions seems to be approximately correct.
Perhaps the MAST source is slightly large
compared to KASSERI.

● Differences between theoretical and observed
amplitudes are less than a factor of two nearly
everywhere. A goodly portion of the discrepancy
can likely be attributed to inaccuracy in the
upper mantle model. More extensive studies em-
ploying much more data could improve this model
and therefore the agreement at individual sta-
tions.

● Changing T/Q from 0.95 to 1.05 increases the
period of the phase measured by ≈ 0.03 - 0.07
seconds. The increase in amplitude is 15 -
25 percent.

● The periods of the b phase generally agree with
the observations. If anything, they may be a
little too short on the average. For the d
phase the theoretical periods tend to be a bit
too long.

● Clearly, the further we go into the record, the
poorer the match between theory and observations.
However, the further one goes into the record,
the greater the effect of factors other than the
coupling of explosion energy into elastic waves.
Hence the emphasis on the b phase.

3.4.4 Surface Wave Predictions for KASSERI and MAST

The first step in our procedure for computing explosion surface waves was to select an appropriate average crustal model for the travel path between NTS and the five SDCS stations. Basically, we began with published models that seemed appropriate, then perturbed them slightly to bring the theoretical group velocity dispersion curves and travel times into close agreement with the observed. The observed curves were computed directly from the MAST observations using the S^3 data analysis program MARS [Savino, et al., 1975]. The dispersion curves for the revised models fit the observations to within 0.04 km/sec for periods between 10 and 30 seconds. The models were CIT109-A for WH2YK, MCEV-J for RKON and MCEV-B for CPSO and FNWV. The published models on which they are based are CIT109 [Archambeau, et al., 1969] and MCEV [McEvilly, 1964]. Only the model MCEV-J differs to any substantial degree from the starting model. For the attenuation we used the model of Tryggvason [1965].

Comparison of the theoretical and observed Rayleigh waves at two (HNME and RKON) of the five SDCS stations are shown in Figure 3.10 for both MAST and KASSERI. The radial and vertical components are both shown. The most important result is, as in the case of the body waves, that the scaling between the synthetic KASSERI and MAST seismograms closely matches the observed scaling. This is important because the body and surface waves sample different portions of the source spectrum and are sensitive to different properties of the source medium. The final point to note is that the agreement between the synthetic and observed seismograms in Figure 3.10 at each of the SDCS stations is well within a factor of two in amplitude and could be improved with more refined travel path models.

26
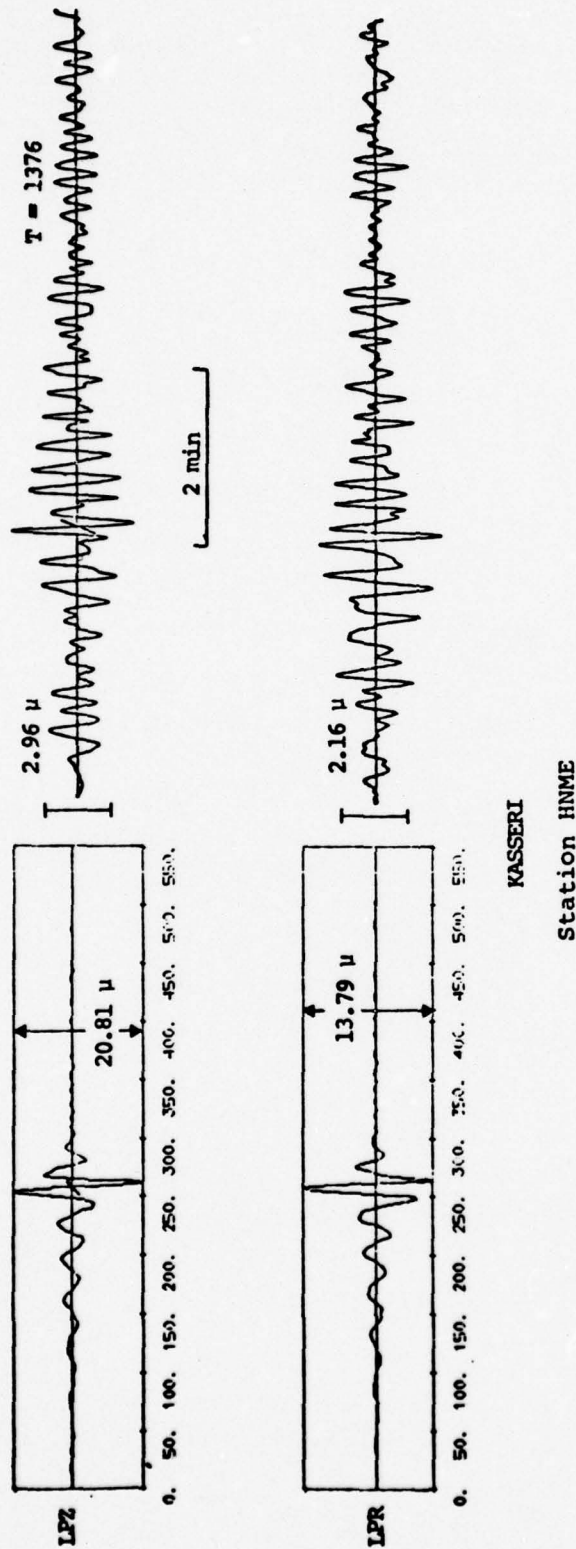
Figure 3.10. Comparison of theoretical and observed Rayleigh waves at five SDCS stations. Both the vertical and radial components are shown for MAST and KASSERI. The amplitude at 25 seconds is indicated on each record. The bar on the vertical records indicates the cycle at which the Airy phase amplitude was measured. The travel time for this phase is indicated on the observations by T. These values, taken from the SDCS event reports, appear to be incorrect in many cases.
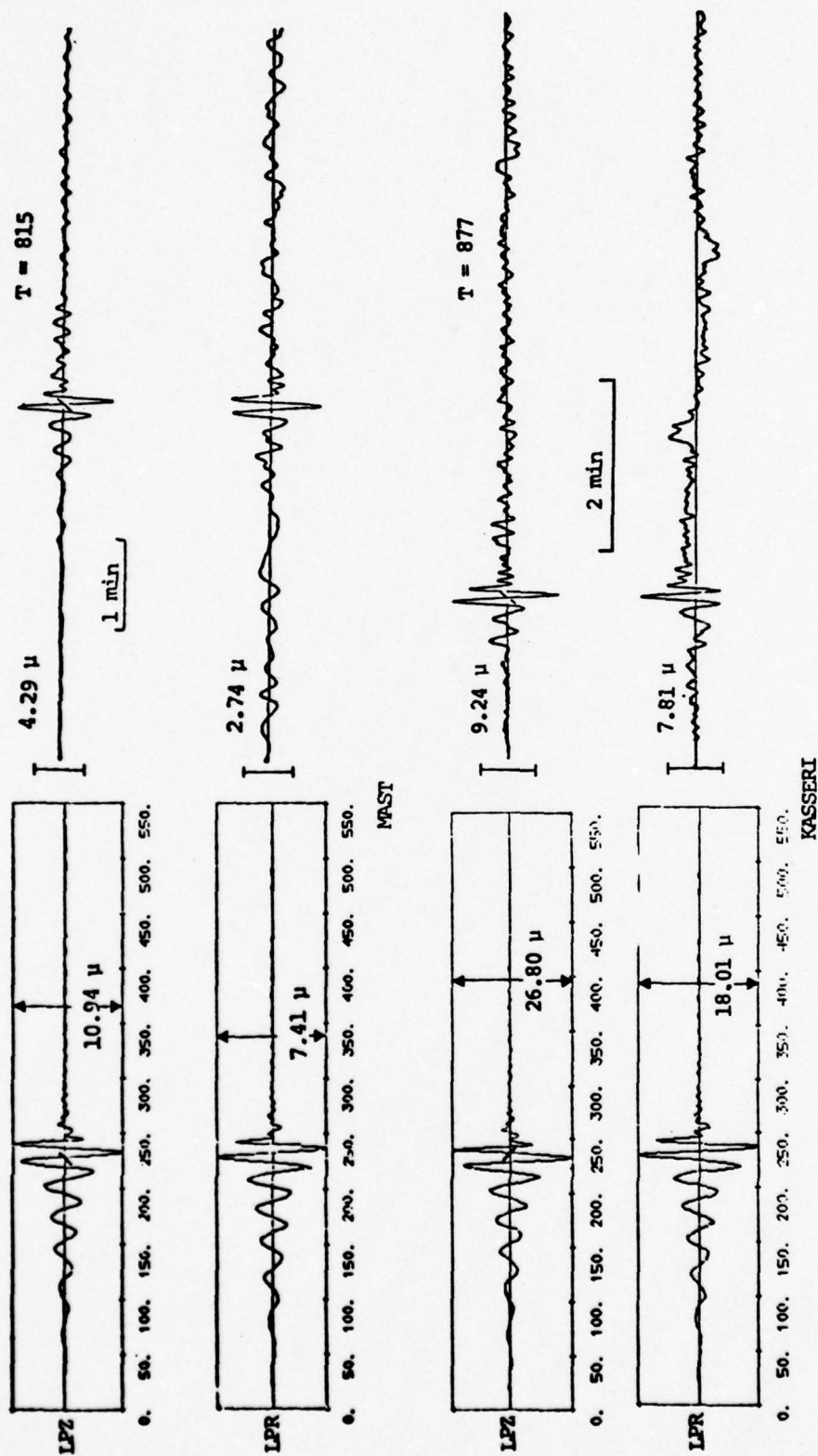
R-3038

Figure 3.10. (Concluded)

28

3.5   TECHNICAL REPORT NO. 6

"Teleseismic Verification of Data Exchange Yields,"
Bache, et al., May, 1976.

3.5.1 Introduction

This report addresses the possibility of directly in-
verting teleseismic ground motion in order to obtain explo-
sion yield. The procedure proposed for accomplishing the
inversion is to employ a deterministic model which predicts
ground motion from a nuclear explosion. This procedure
makes use of the information expected from data exchange
packages that provide information on the near explosion
source environment. Additional parameters must be inferred
from other sources or determined by experiment on geophy-
sical analogues.

This report discusses three major topics: Equivalent
elastic source calculations for a wide range of rock types;
the teleseismic amplitude dependence on the source, including
the effects of the free surface reflected phase, pP, and the
effect of upper mantle elastic properties on short period
P waves.

3.5.2 Equivalent Elastic Source Calculations

Several source calculations, corresponding to an ex-
plosive device yield of 150 kt at a depth of burial of ap-
proximately 560 meters, were carried out. The rock types
considered ranged from a saturated NTS granite to dry shale
and sandstone. Measured material properties for each of the
rock types were used in the source calculations.

Figure 3.11 shows the source functions. Since there
is a factor of ten difference in amplitude at 1 Hz between
the maximum and minimum source functions, it is important
to subdivide these sources into classes. Table 3.2 provides
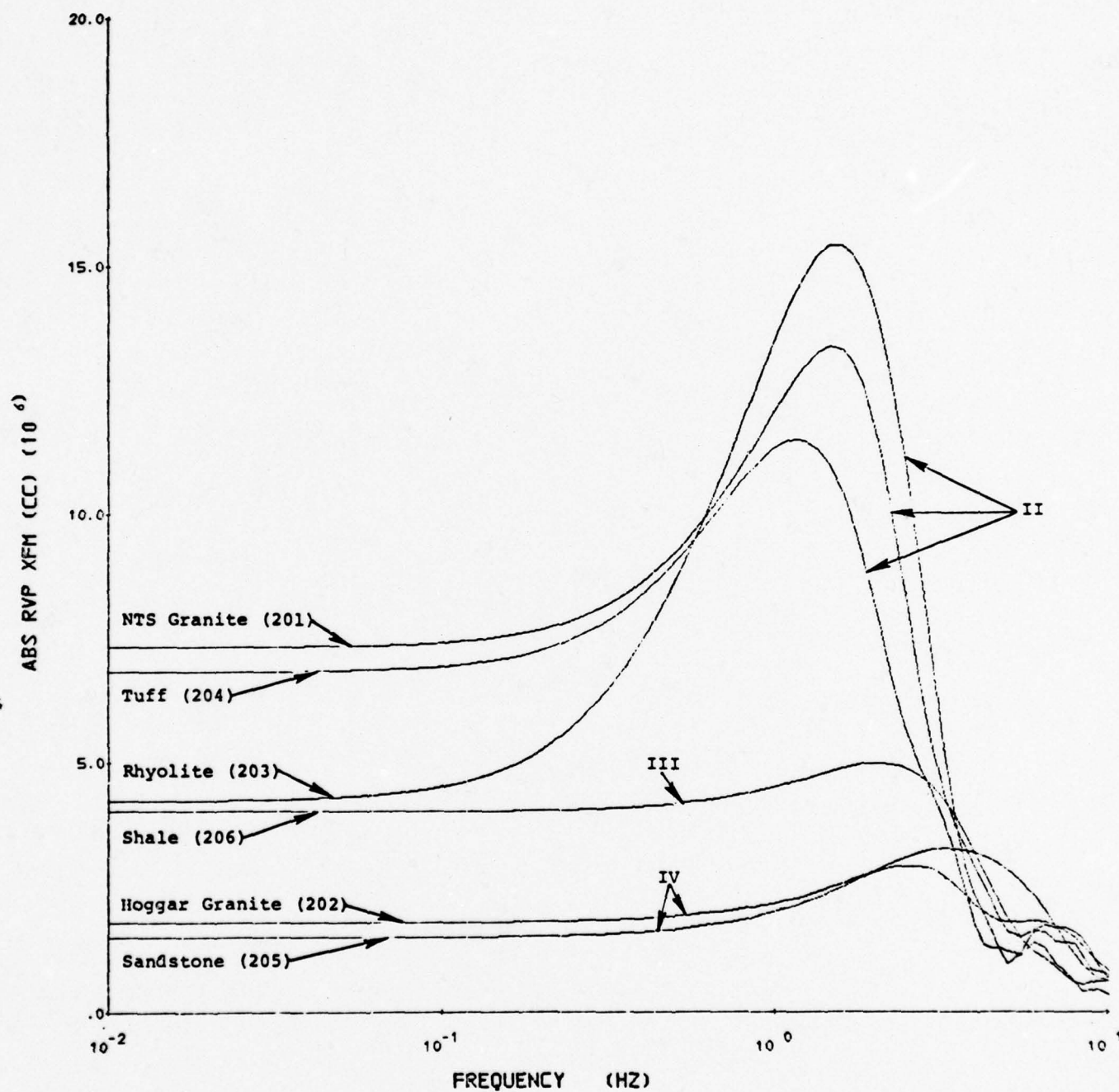
Figure 3.11. Source functions for all rock types except 207.

TABLE 3.2

Calculation	Class	Description	Rock Type	α	μ	$\hat{\hat{\Psi}}$ (1.0)
207	I	Weak, saturated	Tuff	2.4	40	19
201	II	Strong, saturated	Granite	5.3	207	12.0
203	II	Strong, saturated	Rhyolite	4.2	170	13.3
204	II	Strong, saturated	Tuff	3.1	90	11.2
206	III	Weak, dry	Shale	3.9	150	4.5
202	IV	Strong, dry	Granite	5.3	207	2.2
205	IV	Strong, dry	Sandstone	4.3	204	2.0

this separation. This source classification procedure pro-
vides a framework for using data exchange information. The
steps involved are the following:

1. Classify the near source rock environment.

2. Perturb the material properties in the class to
    fit the given depth of burial, density, P wave
    velocity and, hopefully, S wave velocity.

3. Calculate the range of equivalent sources which
    are possible in this class. This range will in-
    clude reasonable variations in material strength
    and air-filled porosity consistent with past ex-
    perience from similar rock types.

3.5.3 Teleseismic Amplitude Dependence on the Source

The question addressed in this section of the report
is how the source spectra translate into short period seismo-
gram amplitudes at teleseismic ranges; that is, into m_b esti-
mates. In order to answer this question, synthetic seismo-
grams were computed for the range of source functions repre-
sented in Figure 3.11. The relative amplitude and frequency
content of these seismograms was dependent only on the
character of the source and source crustal structure, all
other propagation effects held constant. These seismograms
were used to examine the scaling of P wave amplitudes as a
function of source material both with and without the effects
of the free surface included (Figures 3.12 and 3.13).

The important conclusions drawn from this study are:

1. Given the equivalent source, then teleseismic
    ground motion is directly proportional to α.
    The single most important near source material
    property is α.

32
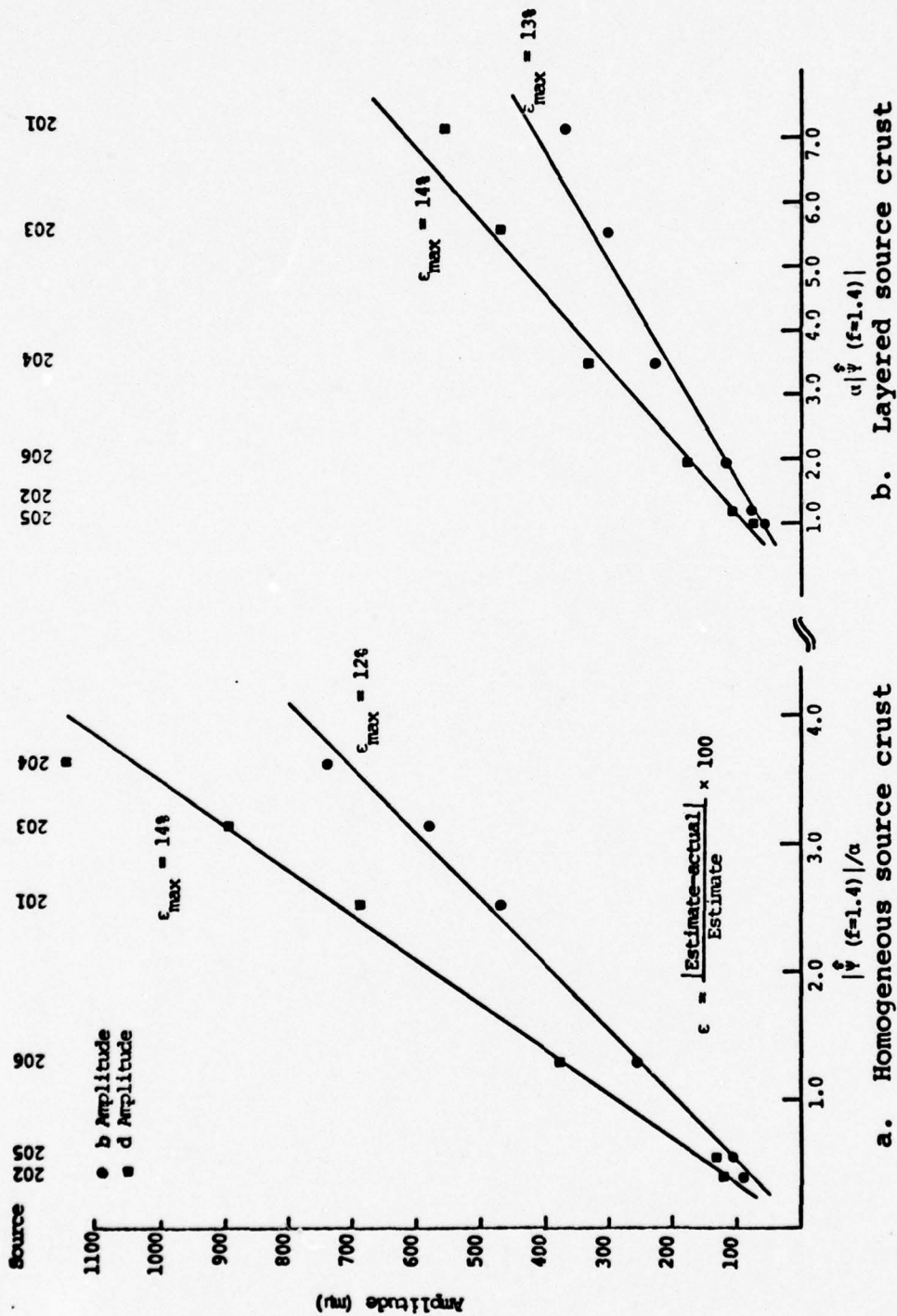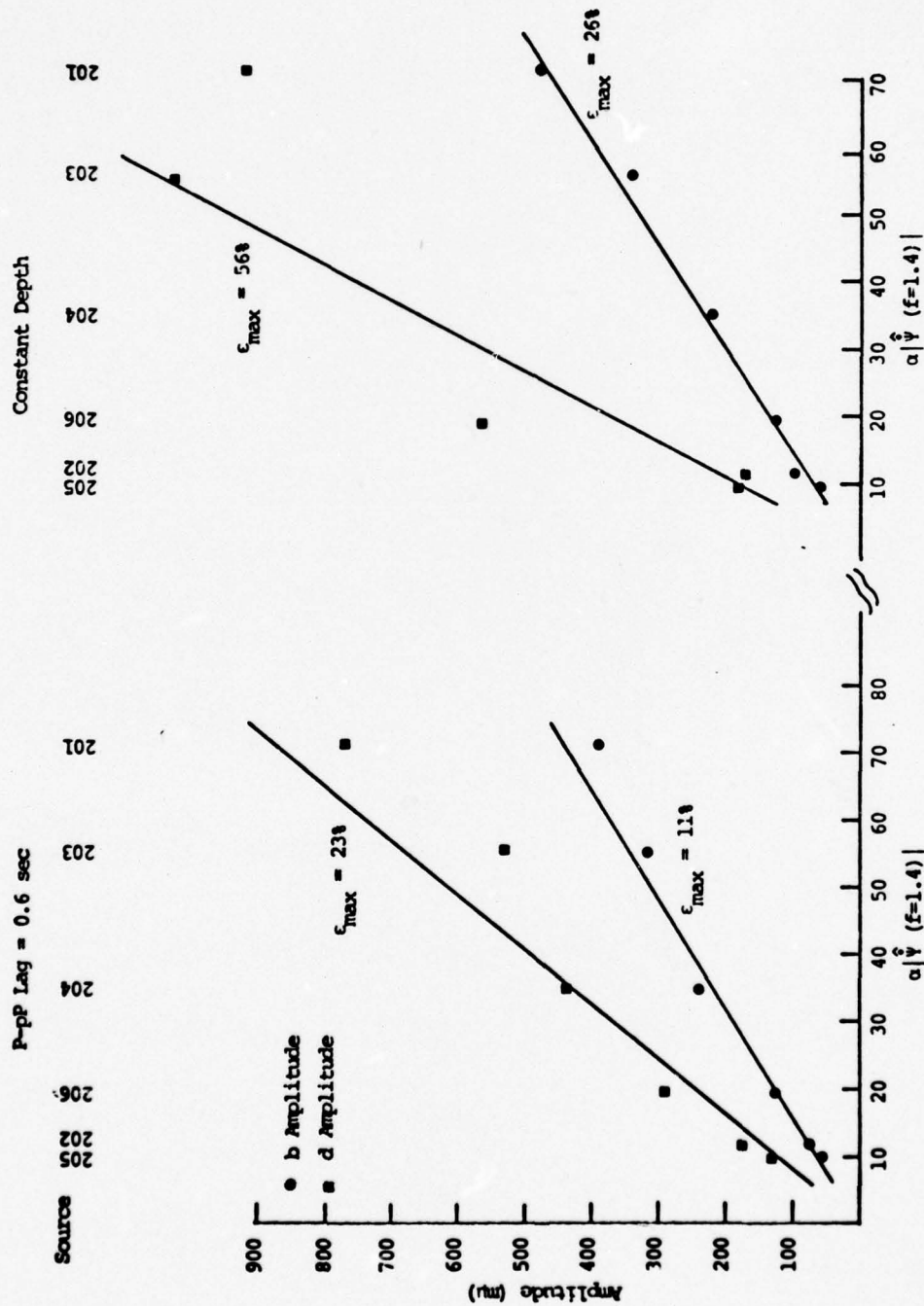
Figure 3.12. Agreement of measured synthetic seismogram amplitudes with theoretical scaling relations. No free surface reflection is included in the calculation.

33

a. Constant P-pP Lag

b. Depth constant; P-pP lag scales with source material velocity.

Figure 3.13. Agreement of measured synthetic seismogram amplitudes with theoretical scaling relations. The free surface effect is included.

2. If possible, use the b amplitude to obtain
    magnitude estimates. For the yields and
    DOB of interest, the b phase is least contami-
    nated by pP.

3.5.4 Effects of Upper Mantle Properties on Short Period Seismograms

The distance range of particular interest here is be-
tween 20° and 36°. In this analysis synthetic seismograms
were computed for this distance range with all factors held
constant except the upper mantle velocity structure. The
example chosen is the MAST explosion in rhyolite.

The upper mantle models studied are perturbations of
models HWNE [Helmberger and Wiggins, 1971] and HWA [Wiggins
and Helmberger, 1973]. The perturbations were not allowed
outside the envelope of all possible models consistent with
travel time, ray parameter and amplitude data for the western
United States, as determined by Wiggins and Helmberger [1974].
The changes from the starting models (which are fairly dif-
ferent from each other) were at most 0.3 km/sec.

Synthetic seismograms appropriate for the epicentral
distance from NTS to the SDCS stations RKON and HNME are
shown in Figures 3.14 and 3.15. These seismograms represent
the extremes of the variation observed at these stations
when perturbing the models under the constraints mentioned
above. The signal at RKON is affected primarily by the
structure 100 km above and below the 400 km discontinuity.
The HNME seismograms are primarily sensitive to the region
below the 600 km discontinuity.

The b and d amplitudes were measured on each seismo-
gram and are listed on Figures 3.14 and 3.15. At the station
RKON, within the triplication range, the ratio of the maxi-
mum to minimum amplitudes is about a factor of 2-2.5, though
the b phase for HWA-3B is exceptionally small. Beyond the
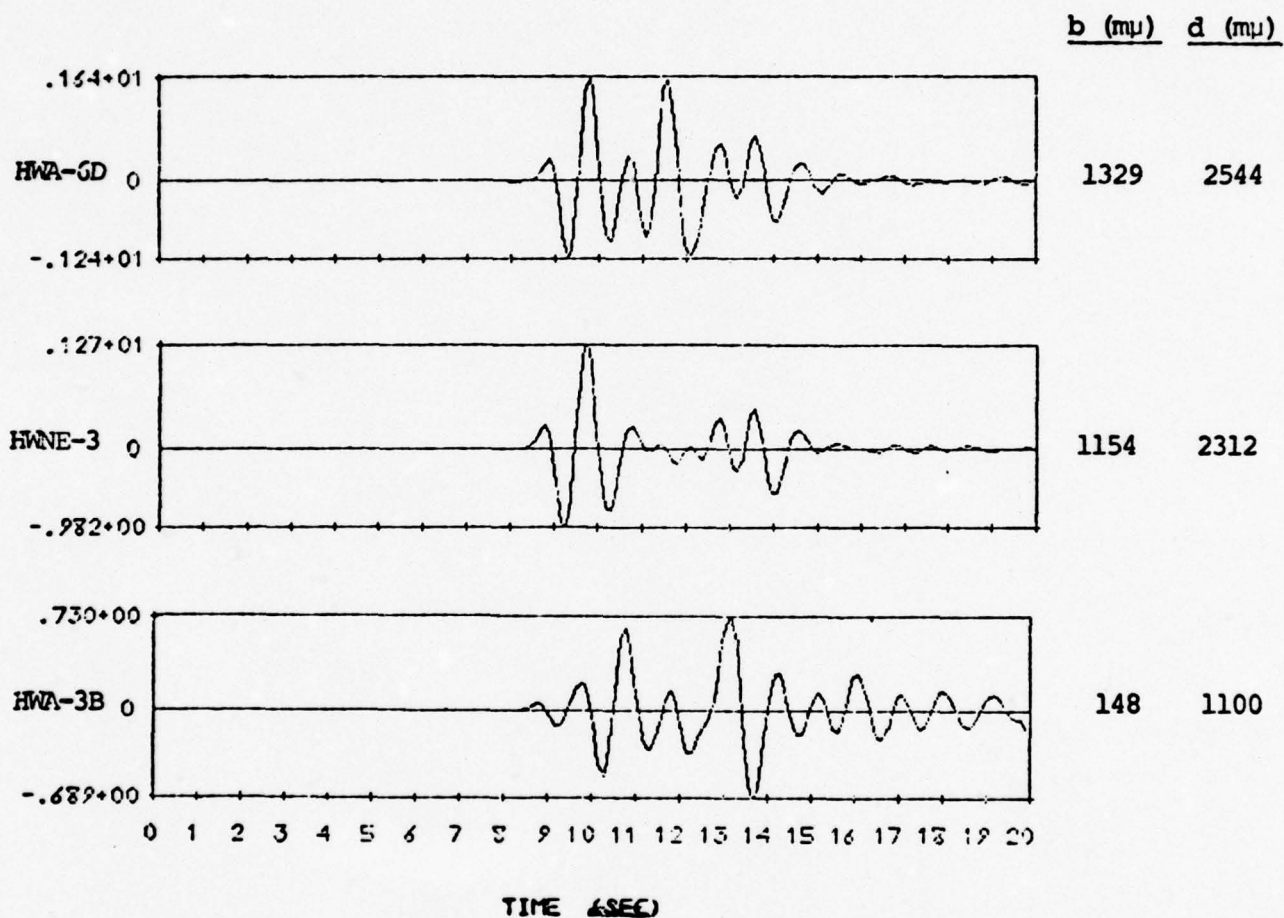
Figure 3.14. Variation in amplitude and waveform for three upper mantle models for MAST at station RKON. For all calculations T/Q = 1.05 and a nominal LRSM response was used.
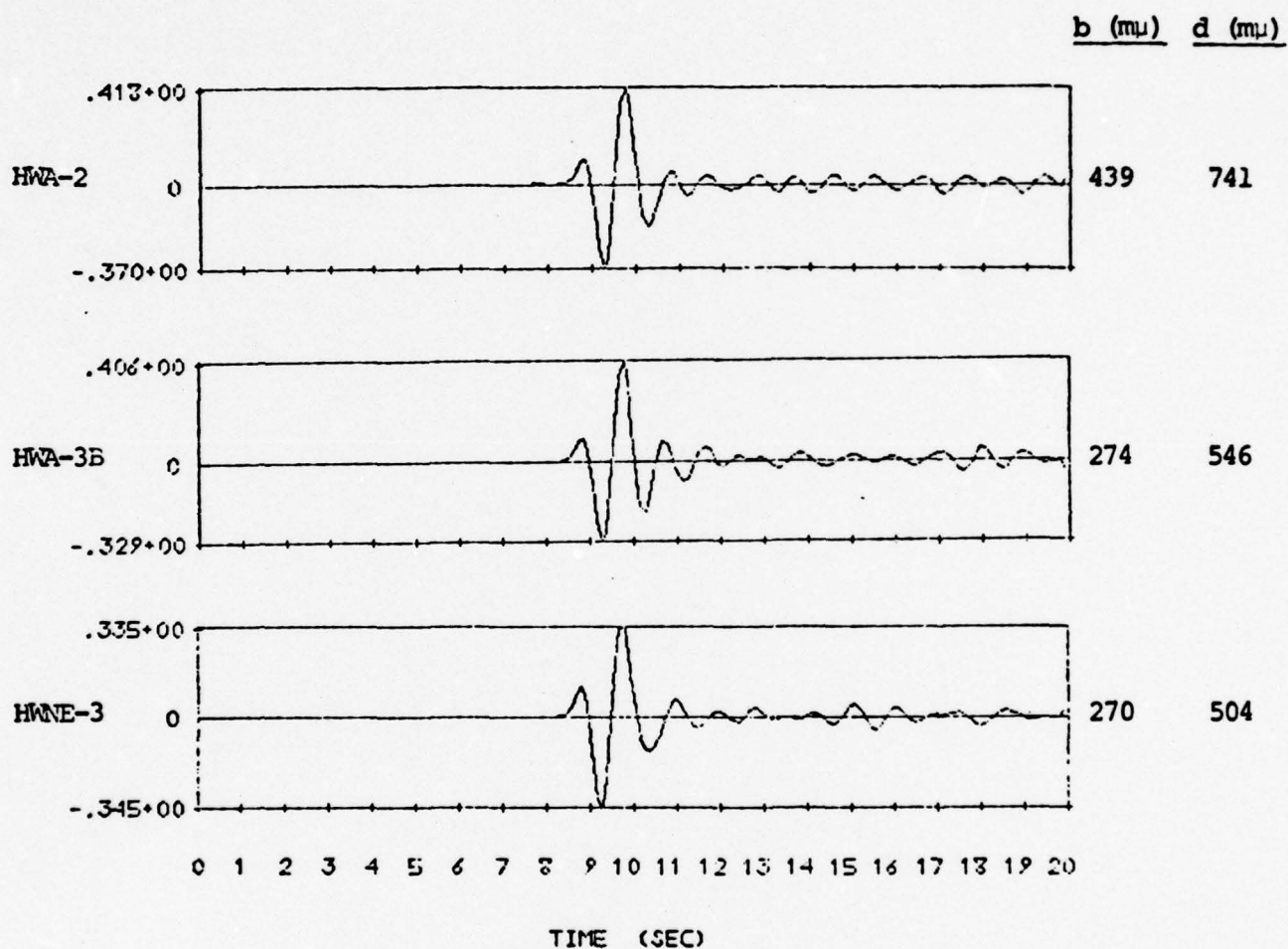
Figure 3.15. Variation in amplitude and waveform for three upper mantle models for MAST at station HNME.

triplications at HNME, the variation is less, a factor of 1.5-1.6.

The small variation in amplitude at the station beyond the triplications is reassuring. It is, to be sure, based on a limited number of model perturbations, but many of these perturbations were designed to change the amplitude at the HNME range. Any model used must be consistent with the available travel time data, etc., and these data severely constrain the velocity profile. If we assume that parallel layered models adequately represent the upper mantle for our purposes, we can be reasonably certain that errors in our knowledge of the velocity-depth profile lead to errors in our computed amplitudes that are on the order of a factor of 1.5 to 1.6.

IV. SUMMARY OF CURRENT RESEARCH

In this section of the report we will briefly summarize the results of work in research areas that were initiated near the end of the reporting period for this contract. This work has not been described in separate Technical Reports.

4.1 EXPLOSION GROUND MOTION PREDICTIONS

The successful prediction of the teleseismic body wave signatures of explosion events involves the following:

1. Computation of the coupling of explosion energy into elastic waves.

2. Constitutive modeling of the behavior of geologic materials over the range of stresses encountered.

3. Propagation of the source-generated elastic waves to teleseismic distances.

In the following subsections we will briefly outline some results on the prediction of ground motion from explosions in different NTS settings.

4.1.1 Source Modeling

In Figure 4.1 we show the equivalent elastic source for explosions detonated in a variety of NTS emplacement materials. The source function is $\hat{\psi}(\omega)$, a Fourier transformed quantity that is related to the far-field displacement spectrum, $\hat{u}(\omega)$, in a whole space by

$$\hat{u}(\omega) = \frac{\hat{\psi}}{R\alpha},$$

where R is distance and α is P wave velocity. The key parameters distinguishing the calculations are listed in Table
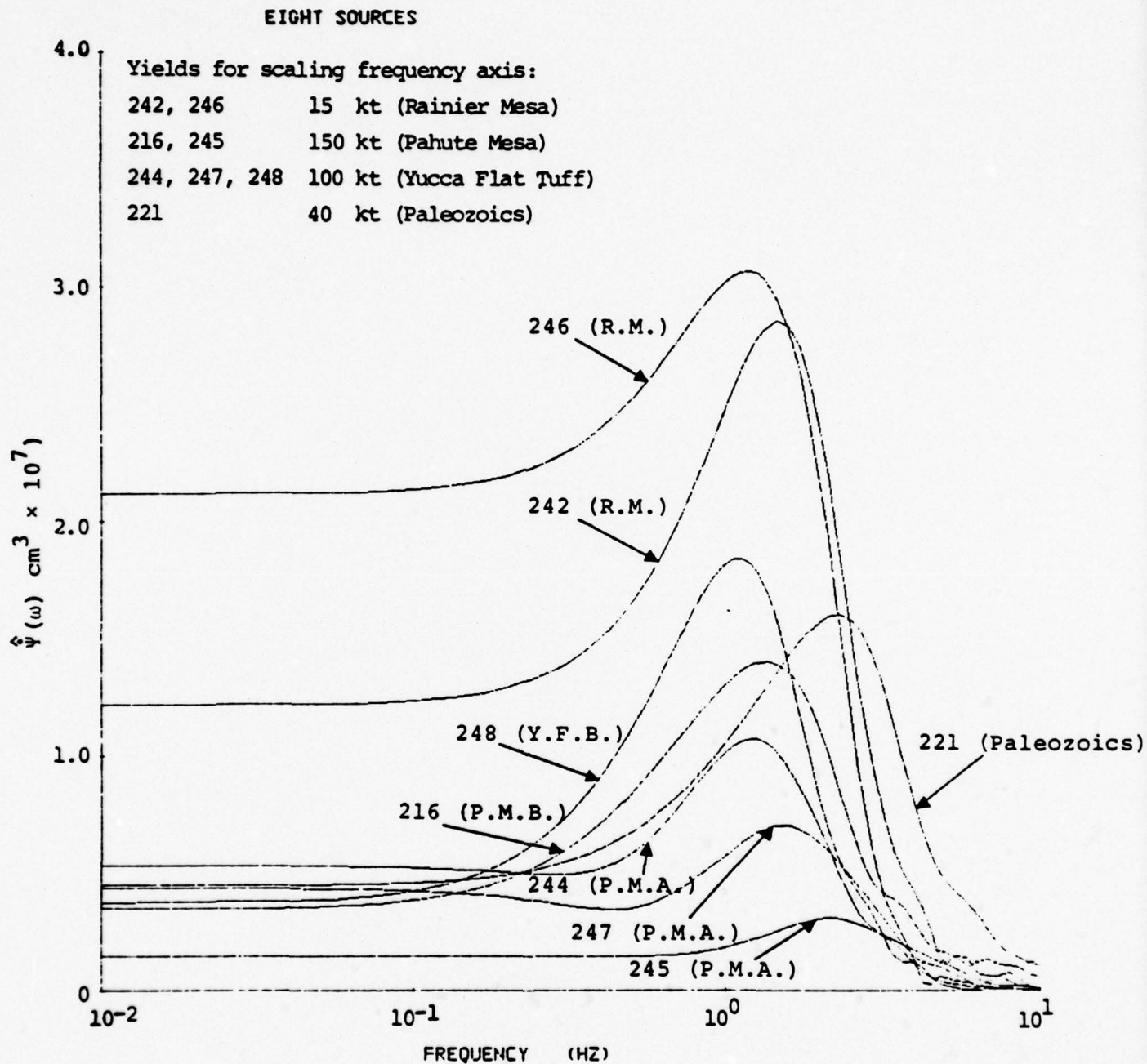
39

EIGHT SOURCES

Figure 4.1. Source functions for the materials specified in
Table 4.1. The amplitude axis is scaled to 0.02
kt while the frequency axis is cube-root scaled
to the yield indicated for each source.

40

4.1. They are the elastic properties, density (ρ) and velocities (α, β), the air-filled porosity (ϕ_0), and the failure envelope parameters, Y_0, Y_m and $\overline{P}_m$. Briefly, we have

$$\overline{P} = P - \frac{1}{2}\left(\frac{J_3'}{2}\right)^{1/2}$$

where P is the pressure including the overburden and J_3' is the third deviatoric stress invariant. The meaning of the parameters Y_0, Y_m and $\overline{P}_m$ is illustrated in Figure 4.2.

In Figure 4.1 we see that the source functions vary over a considerable range of amplitudes for far-field yield. The body wave magnitude is related to the source function amplitude (to first order) by $m_b \approx \alpha \hat{\Psi}(f_0)$, where $f_0 \approx 1$ Hz. The m_b is clearly dependent on local material properties as well as explosion yield.

4.1.2 Theoretical Seismograms

The source functions of Figure 4.1 were used to synthesize short period seismogram recordings of NTS events in the appropriate materials. The yield and depth of burial of these events were also known. We had previously developed good velocity and Q models for the travel path between NTS and a receiver station at teleseismic distances which obtained good recordings of these events.

The comparison between synthetic and actual seismograms at a particular station is shown in Figure 4.3 for seven NTS explosions. The synthetic seismograms include the interference effects of the free surface reflected phase, pP. The agreement between the predicted (light line) and observed (heavy line) seismograms is quite striking. For all seven explosions, both the absolute amplitude and frequency content of the waveforms have been matched, providing confirmation of the deterministic modeling approach adopted.

41

Y

$Y_0 + Y_m$

Shock Loading

$1-2\sigma$
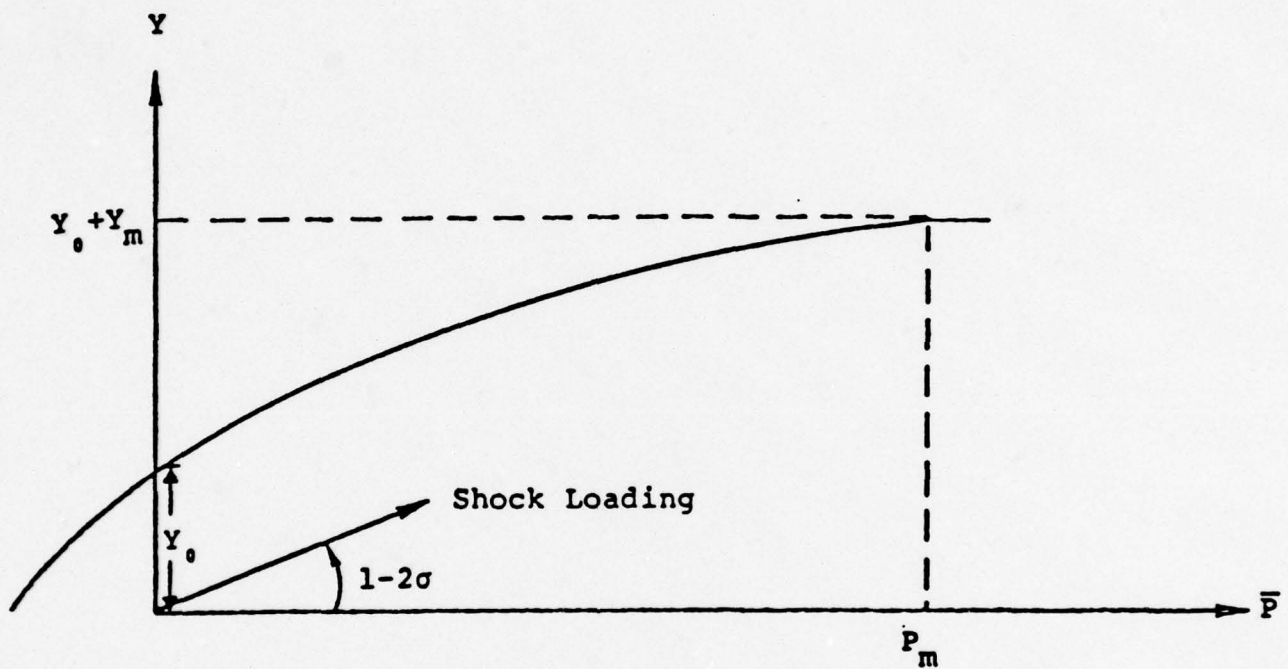
Y_0

$\overline{P}$

P_m

Figure 4.2. Assumed relationship between the material strength
(Y) and the hydrodynamic component of stress ($\overline{P}$)
for small e/e_m. When $\overline{P}$ is used for the abcissa
the shock loading path has a slope of $1-2\sigma$.

TABLE 4.1
MATERIAL PROPERTIES USED IN SOURCE CALCULATIONS

Rainier Mesa

ρ	α	β	ϕ_0	Y_0	Y_m	$\overline{P}_m$	Source
1.9	2.5	1.3	1.36	0.05	1.45	2.9	242
				0.05	0.35	2.0	246

Pahute Above

ρ	α	β	ϕ_0	Y_0	Y_m	$\overline{P}_m$	Source
1.91	3.28	1.9	14.5	0.115	3.1	4.7	245

Pahute Below

ρ	α	β	ϕ_0	Y_0	Y_m	$\overline{P}_m$	Source
2.19	3.4	2.1	0	0.16	4.3	5.6	216

Yucca Above

ρ	α	β	ϕ_0	Y_0	Y_m	$\overline{P}_m$	Source
1.78	1.8	1.0	14.0	0.03	0.77	1.54	244
				0.15	0.6	2.0	247

Yucca Below

ρ	α	β	ϕ_0	Y_0	Y_m	$\overline{P}_m$	Source
1.86	2.35	1.3	3.0	0.05	1.45	2.9	248

Paleozoic

ρ	α	β	ϕ_0	Y_0	Y_m	$\overline{P}_m$	Source
2.78	5.45	3.1	0	0.34	12	14.1	221, 222
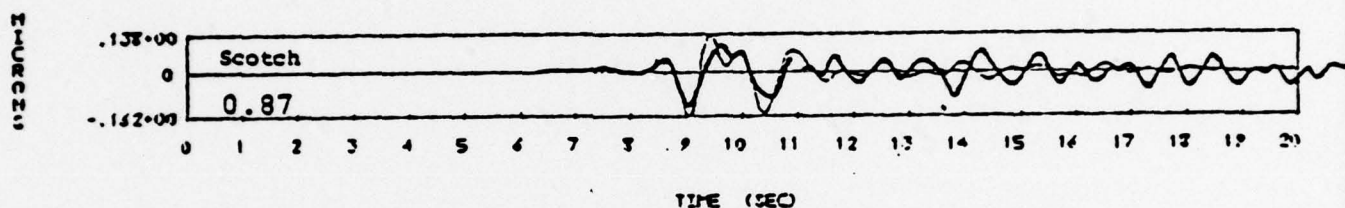
Pahute Mesa Below the Water Table

Figure 4.3.   Comparison of synthetic and actual (heavy line)
short-period vertical recordings of NTS explo-
sions at a range > 3500 km. The delay time
between the P and pP phase for the calculations
is indicated on each record.
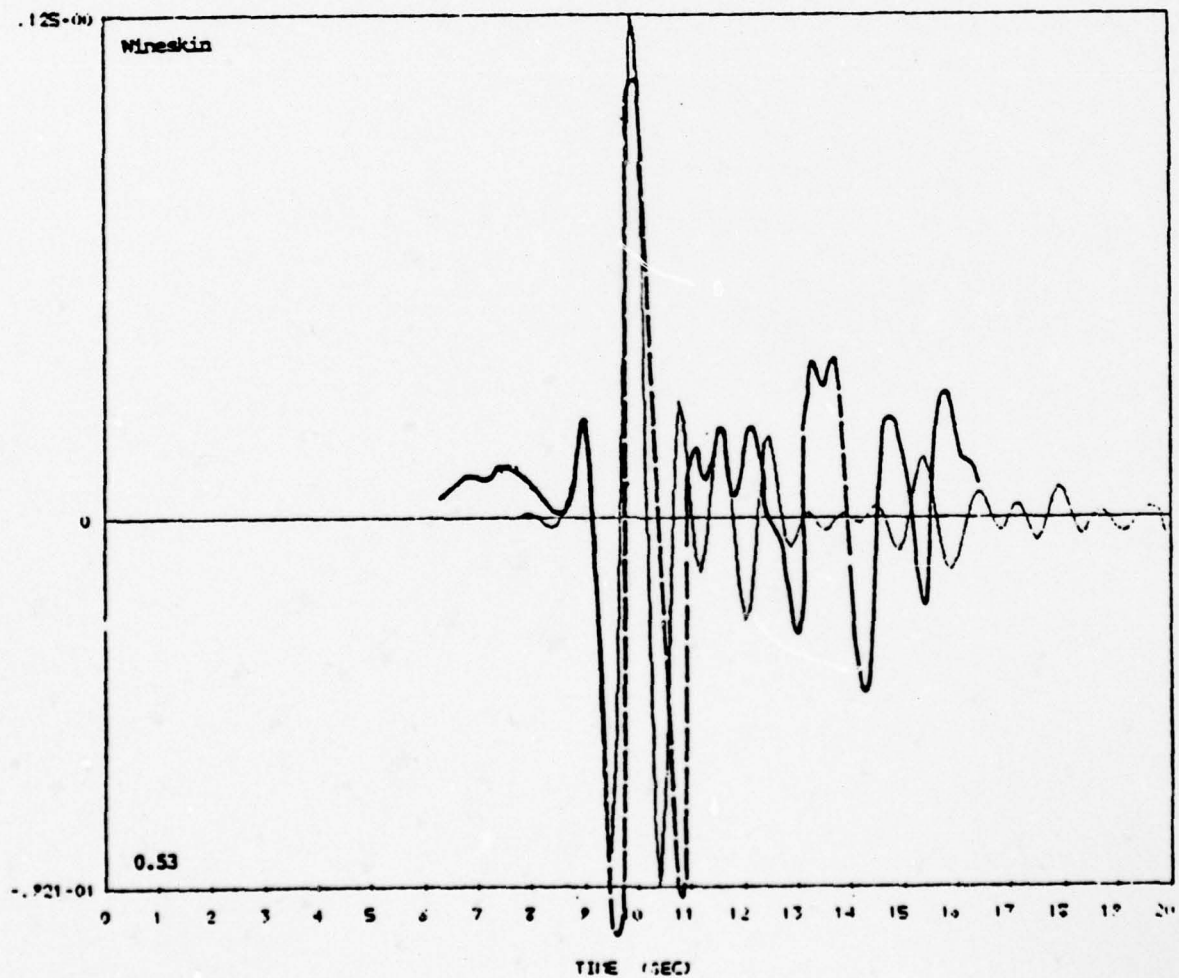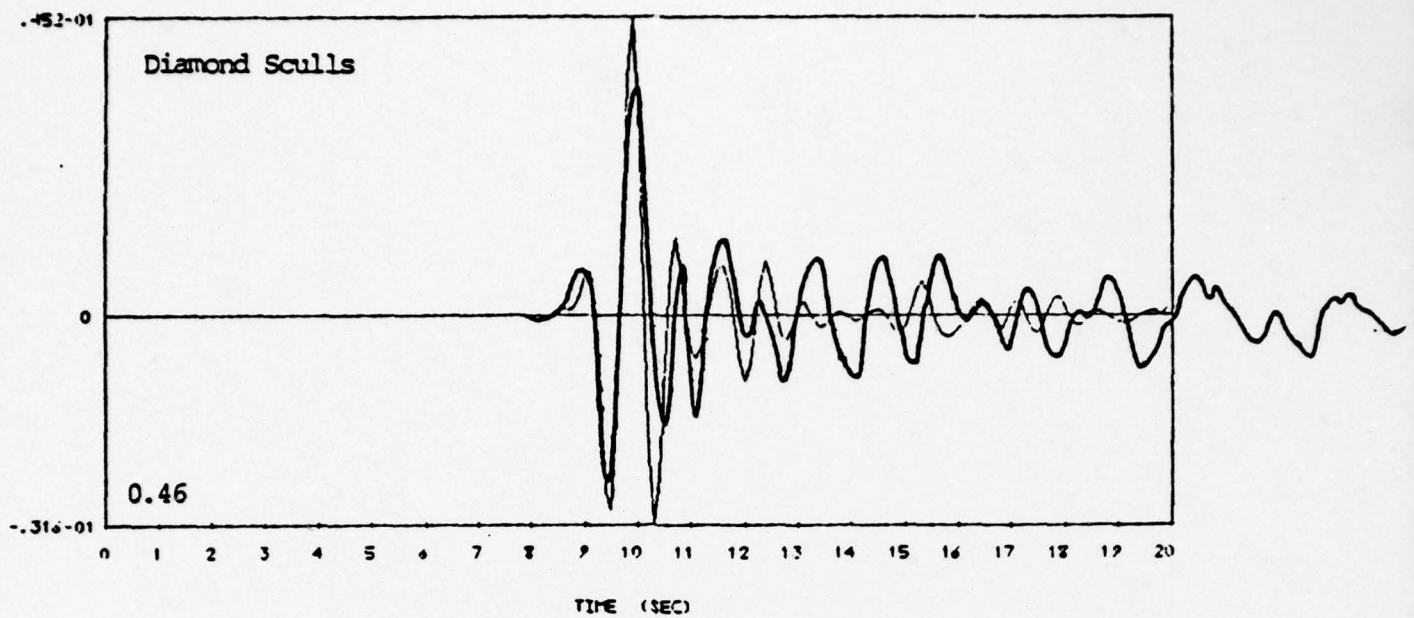
Seismograms for Rainier Mesa Events
(Source 242)

Yucca Flat Below Water Table

Paleozoics at Yucca Flat

Figure 4.3 (Concluded)

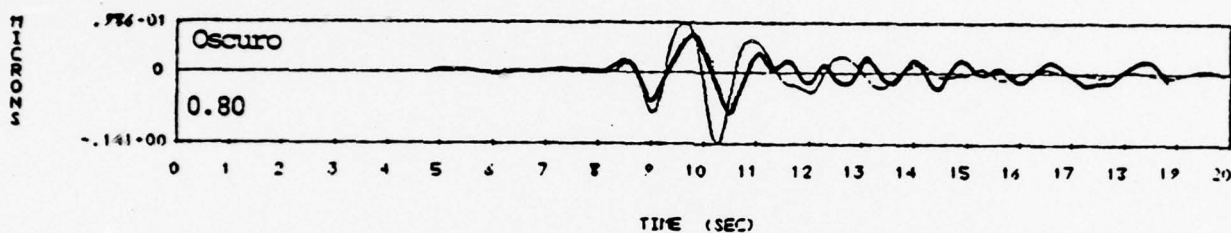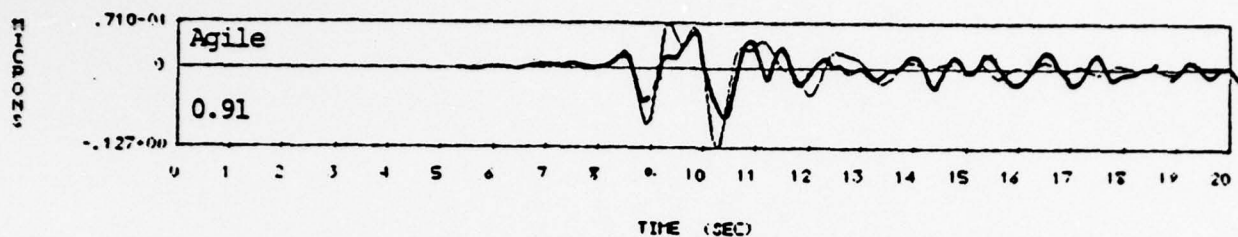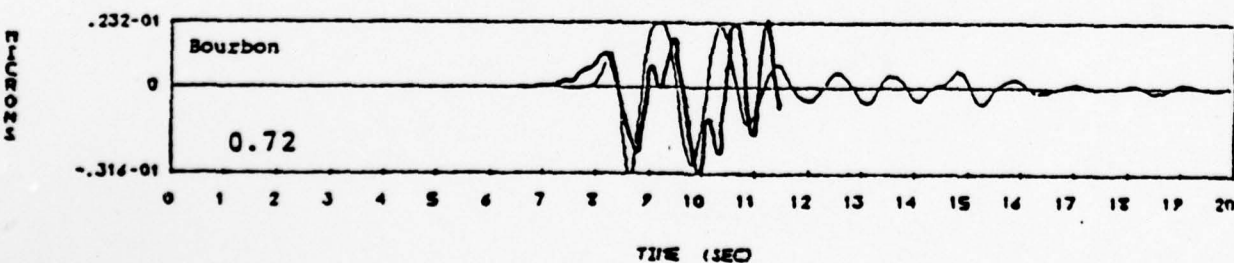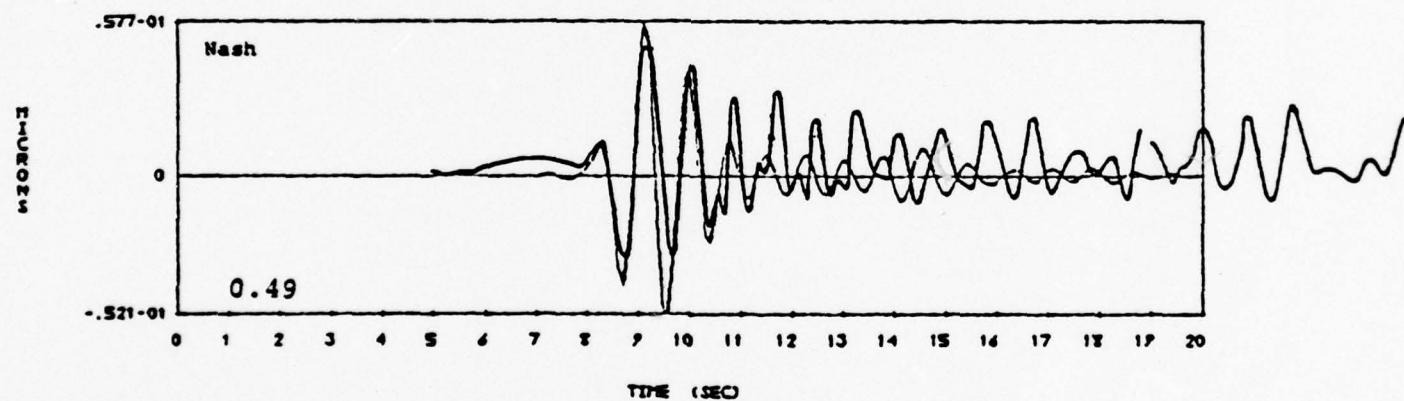## 4.2   SIMULATION AND DECOMPOSITION OF MULTIPLE EXPLOSIONS

4.2.1   Introduction

Recently, we began experimenting with computer simulation and decomposition of multiple explosion scenarios. The objectives of this experiment are to develop procedures, based on close-in seismic measurements, for verifying the number and yields of individual explosions comprising a multiple event. We are also interested in detecting explosions that are detonated concurrently with a multiple event but are located outside the array.

4.2.2   Experiment Design and Data

The data selected for the first multiple event scenario consisted of close-in seismic measurements of the single, contained, underground explosion MAST detonated June 19, 1975, in the Pahute Mesa region at NTS. These data were obtained in digital format from Sandia Laboratories in Albuquerque, New Mexico, and include accelerometer and velocity gauge seismograms recorded in the distance range from ground zero to about 9 kilometers from MAST. The digital data were sampled at a rate of 500 points per second.

The explosion and recording station configuration used for the simulated multiple event are shown in Figure 4.4. The test scenario consisted of a linear array of three equivalent yield explosions, equally spaced (355 m) and detonated simultaneously. The explosion spacing of 355 m was taken as representative of row cratering shots in the yield range near 150 kt.

In the numerical simulations to be discussed herein, actual vertical component velocity recordings of the MAST explosion were used. The simulated composite velocity seismograms were constructed at each of the stations along the in-line and 45° profiles shown in Figure 4.4 by delaying

Figure 4.4. Explosion and station configuration.

and summing the actual MAST seismograms recorded at the
(approximate) corresponding distances. The delays were
based on the spacings between shots, the propagation
velocity assumed and the azimuth to the recording station.

An example of the construction of a seismogram for a
multiple event is given in Figure 4.5. This seismogram is
for Station 3 along the in-line profile. On the left-hand
side of Figure 4.5 we show the actual vertical component
velocity seismogram recorded at Station 3 for MAST. The dis-
tance range in this case is 0.912 km. The multiple explo-
sion time series is shown on the right-hand side of Figure
4.5. Comparing the original and composite signals we see
that, except for the change in peak-to-peak signal amplitude,
the superposition of the delayed signals from the three
explosions results in only subtle changes in the shape of
the waveform. It is quite likely that an analyst would not
interpret this seismogram as that from a multiple explosion.

4.2.3 Experimental Results for the Profile of Stations In-Line with the Explosion Array

In Figure 4.5 we showed the original velocity record
for Station 3 located 0.912 km from MAST. We also showed the
composite or summed velocity record for Station 3 on the
profile in-line with the three shots. The delays are based
on the spacing between shots (355 m) and a velocity of 3.8
km/sec. Hence, delay times of 0.093 seconds are appropriate
(0.355 km/3.8 (km/sec) = 0.093 sec) for all stations along
this profile.

A series of 16 narrow band filters with center fre-
quencies (f_c) ranging from 25 to 100 Hz was applied to both
the original and composite signal shown in Figure 4.5. The
time series output from these filters is shown in Figure 4.6.
For the original MAST record at Station 3, three major
bursts of high frequency energy occur for this band of

Original Time Series

Summed Time Series

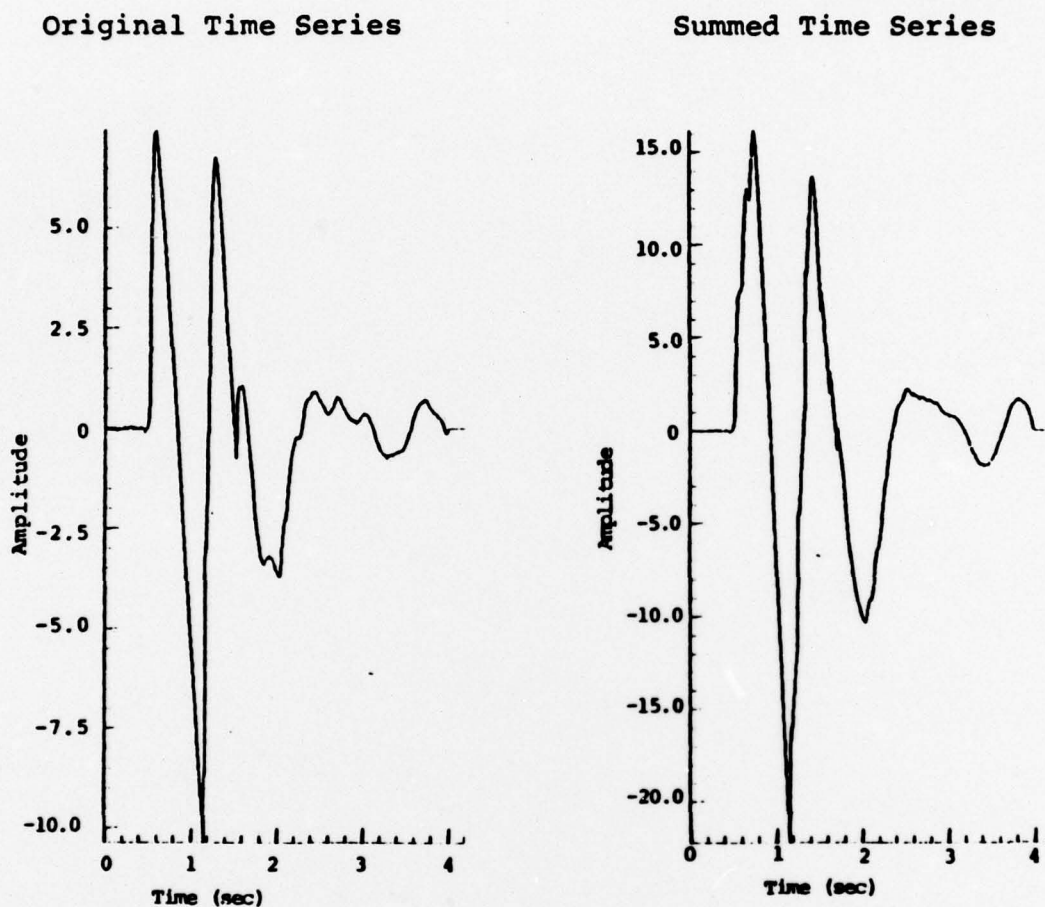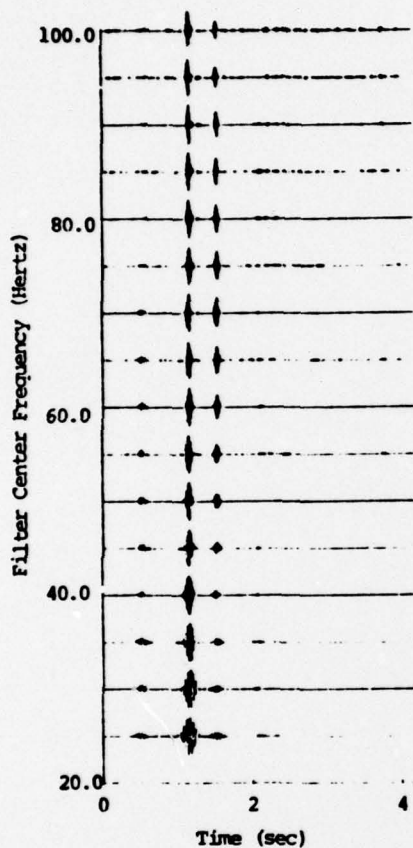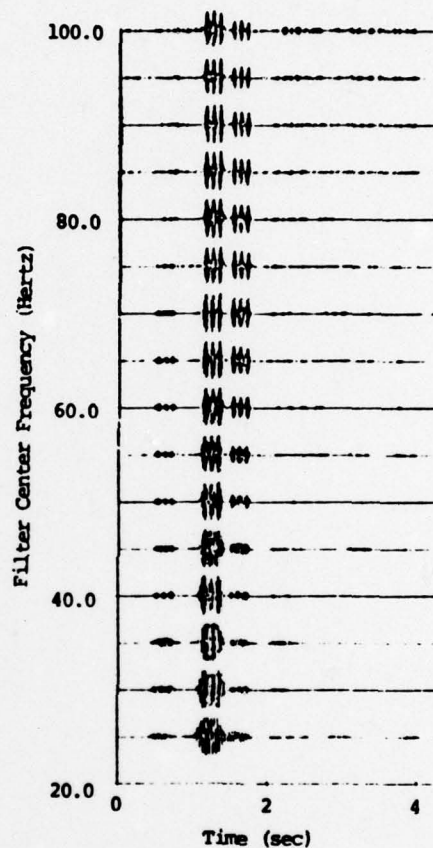Figure 4.5.   Original MAST signal at Station 3 and composite
signal along the profile in-line with the shot
array.

**Filtered Signal
- Original Signal**

**Filtered Signal
- Composite Signal**

(a)

(b)

Figure 4.6. Narrow band filtered signals (as functions of frequency and time) for the original (a) and composite (b) signals for Station 3 (Figure 4.5) along the profile in-line with the shot array.

51

frequencies (Figure 4.6a). The times are 0.55, 1.2 and 1.55 seconds. Since we have not attempted to interpret these records, we will not attempt to discuss the origin of these high frequency energy bursts. However, the important fact remains that there is a high signal-to-noise ratio (S/N) at these frequencies. The significance of this result is shown in Figure 4.6b when the same set of filters is applied to the composite (three explosions) event. Here the three major high frequency bursts of energy now show triple peaks where before there was only one. Separation begins at about 40 Hz and becomes increasingly clear at higher frequencies.

Using the Hilbert transform described in Savino, et al. [1975], envelope functions were constructed for each of the sixteen filter outputs. The envelope functions are shown in Figure 4.7a and b for the original and composite signals, respectively. The important point to note (Figure 4.7b) is the clear separation of the three arrivals, corresponding to the three explosions in the scenario. This separation is even more dramatic in Figure 4.8b, where the sum of the envelopes at the different frequencies (Figure 4.7b) is plotted for the composite signal. A similar sum is plotted for comparison in Figure 4.8a for the original signal.

The time separations of the maximum power arrivals between 1.0 and 1.4 seconds in Figure 4.8b correspond as well as can be determined to the time delays (0.093 seconds) associated with the equal spacings of the three simulated bombs. In addition, note that while the amplitude of the composite signal in Figure 4.5 is more than twice the amplitude of the original signal in Figure 4.5, each peak in the composite envelope sum is nearly equal in amplitude to the peak amplitude of the original unsummed signal.

Similar results are obtained for Stations 2 and 4 in this profile. Again, three major high frequency energy levels are observed. Separation due to the three explosions

Filter Envelopes
- Original Signal
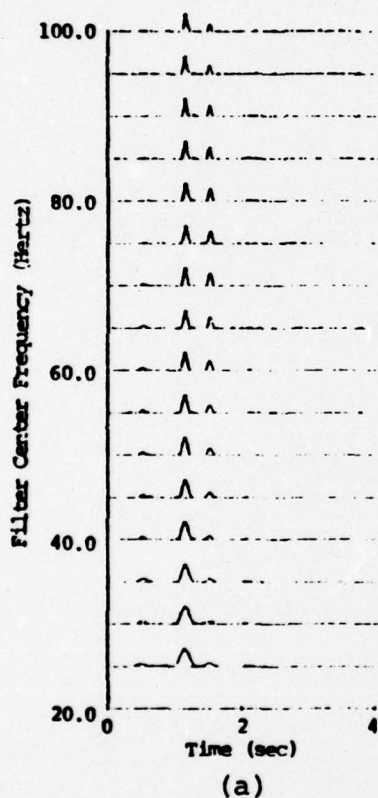
Filter Envelopes
- Composite Signal

(a)

(b)
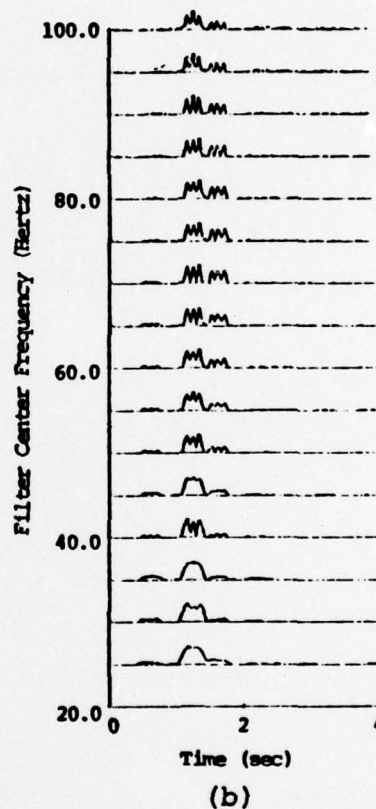
Figure 4.7. Envelope functions (as functions of frequency and time) for narrow band filtered original (a) and composite (b) signals for Station 3 (Figure 4.4) along the profile in-line with the shot array.

53

Sum of Envelopes
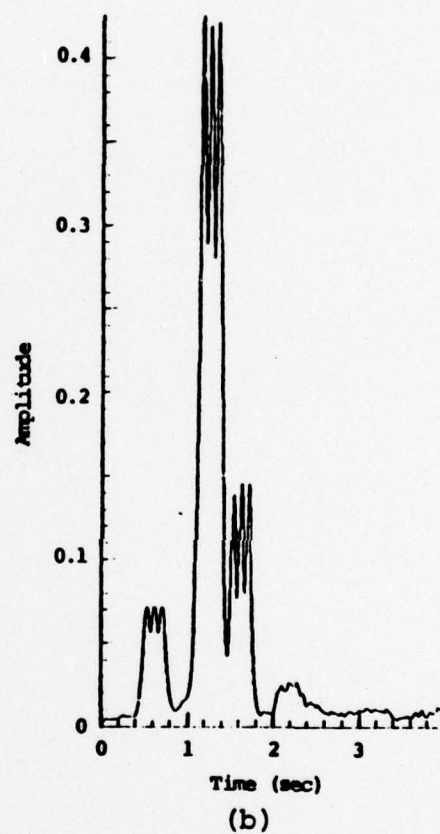- Original Signal
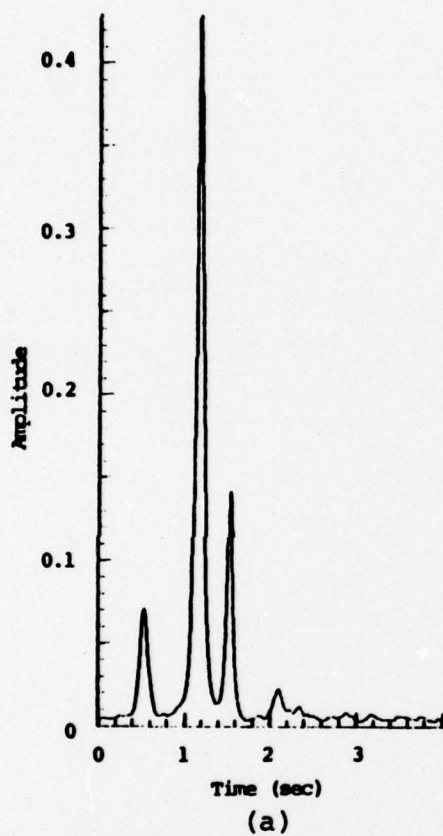
Sum of Envelopes
- Composite Signal

Figure 4.8.   Sum of the envelopes shown in Figure 4.7 for
the original (a) and composite (b) signals for
Station 3 along the profile in-line with the
shot array.

occurs at about 40 Hz and becomes more distinct with increas-
ing frequency. Average time separation of the triple peaks
is 0.093 and 0.093 seconds, respectively. The observed de-
lay times correspond almost exactly to the input delay times
(Table 4.2).

For Stations 5, 6 and 7, high frequency noise dominates
the records and the high frequency signal energy, if present,
is too low level to obtain any definitive results.

4.2.4 Experimental Results for the Profile of Stations 45° from the Explosion Array

Composite or summed seismograms were synthesized for
the stations oriented at a 45° azimuth from the explosion
array. Delay times were determined relative to the center
explosion position (number 2 in Figure 4.4) and are listed
in Table 4.2. The delay times vary and are less than those
for the in-line array. At those Stations (2-4) where noise
was not a problem, the input and observed delays agree to
1 msec or better.

4.2.5 Summary and Discussion

Close-in seismic data obtained from Sandia for the
underground nuclear explosion MAST have been used to simulate
a simple multiple explosion. This multiple explosion con-
sisted of three equal sized (150 kt) aligned explosions
(separated by 355 m) detonated at the same instant. Two
profiles were simulated, one in-line with the explosion array
and the other oriented at 45° to the explosion array. Seismic
records for the multiple event were synthesized by simple
summation of one MAST seismic record to the same record with
appropriate delay times. The determination of the delay
times was based on the orientation of the two hypothetical
station arrays relative to the explosion array, actual sta-
tion distances from MAST and a compressional velocity of
3.8 km/sec.

TABLE 4.2

INPUT DELAY TIMES VERSUS OBSERVED DELAY TIMES

Shot / Station	Input Delay Times For Stations In-Line With Shot Array (sec)		Observed Delay Times For Stations In-Line With Shot Array (sec)		Input Delay Times For Stations Along 45° Profile Relative to Shot #2 (sec)		Observed Delay Times For Stations Along 45° Profile Relative to Shot #2 (sec)	
	1-2	2-3	1-2	2-3	1-2	2-3	1-2	2-3
2	0.093	0.093	0.091	0.093	0.034	0.076	0.034	0.076
3	0.093	0.093	0.093	0.092	0.053	0.072	0.052	0.073
4	0.093	0.093	0.092	0.093	0.061	0.069	0.060	0.070
5	0.093	0.093	—	—	0.062	0.067	—	—
6	0.093	0.093	—	—	0.063	0.066	—	—
7	0.093	0.093	—	—	0.064	0.066	—	—

Application of a series of cusp-shaped narrow band
filters, with center frequencies (f_c) ranging from 25 Hz to
160 Hz, to the synthesized multiple explosion records
yielded the following results:

- Accurate relative amplitude and time separation
  between explosions was achieved at the very
  close stations and, in particular, at distances
  of less than 1.5 kilometers. Beyond 1.5 kilometers
  the signal-to-noise ratio is too low in the high
  frequency band of analysis to obtain definitive
  results.

- Separation between explosions was observed to
  begin at frequencies 3.5 times the explosion
  frequency (inverse of the explosion delay times).
  In general, separation of events becomes more
  distinct with increasing frequency.

V. REFERENCES

Archambeau, C. B., E. A. Flinn and D. G. Lambert [1969], "Fine Structure of the Upper Mantle," J. Geophys. Res., 74, pp. 5825-5865.

Bache, T. C., J. T. Cherry, K. G. Hamilton, J. F. Masso and J. M. Savino [1975a], "Application of Advanced Methods for Identification and Detection of Nuclear Explosions from the Asian Continent," Systems, Science and Software Semi-Annual Technical Report, AFOSR, SSS-R-75-2646, May.

Bache, T. C., J. T. Cherry, N. Rimer, J. M. Savino, T. R. Blake, T. G. Barker and D. G. Lambert [1975b], "An Explanation of the Relative Amplitudes of the Tele- seismic Body Waves Generated by Explosions in Dif- ferent Test Areas at NTS," Systems, Science and Software Final Report, DNA, SSS-R-76-2746, October.

Cherry, J. T., T. C. Bache and D. F. Patch [1975a], "The Teleseismic Ground Motion Generated by a Nuclear Explosion Detonated in a Tunnel and Its Effect on the M_s/m_b Discriminant," Systems, Science and Software Final Report, DNA 3958F, May.

Cherry, J. T., T. C. Bache and W. O. Wray [1975b], "Tele- seismic Ground Motion from Multiple Underground Nuclear Explosions," Systems, Science and Software Technical Report, AFTAC/VSC, SSS-R-75-2709, September.

Garg, S. K. and A. Nur [1973], "Effective Stress Laws for Fluid-Saturated Porous Rocks," J. Geophys. Res., 78, pp. 5911-5921.

Garg, S. K., D. H. Brownell, Jr., J. W. Pritchett and R. G. Herrmann [1975], "Shock-Wave Propagation in Fluid- Saturated Porous Media," J. Appl. Phys., 46, pp. 702- 713.

Helmberger, D. V. and R. A. Wiggins [1971], "Upper Mantel Structure of the Midwestern United States," J. Geophys. Res., 76, pp. 3229-3245.

McEvilly, T. V. [1964], "Central U. S. Crust-Upper Mantle Structure from Love and Rayleigh Wave Velocity Inversion," Bull. Seism. Soc. Am., 54, pp. 1997-2016.

Savino, J. M., T. C. Bache, J. T. Cherry, K. G. Hamilton,
      D. G. Lambert and J. F. Masso [1975], "Application
      of Advanced Methods for Identification and Detection
      of Nuclear Explosions from the Asian Continent,"
      Systems, Science and Software Semi-Annual Technical
      Report, AFOSR, SSS-R-76-2792, December.

Tryggvason, E. [1965], "Dissipation of Rayleigh Wave Energy,"
      J. Geophys. Res., 70, pp. 1449-1455.

Wiggins, R. A. and D. V. Helmberger [1973], "Upper Mantle
      Structure of the Western United States," J. Geophys.
      Res., 78, pp. 1870-1888.

Wiggins, R. A. and D. V. Helmberger [1974], "Synthetic
      Seismogram Computation by Expansion in Generalized
      Rays," Geophys. J., 37, pp. 73-90.

APPENDIX A

LIST OF REPORTS FROM CONTRACT NO.
F08606-75-C-0045

A. QUARTERLY REPORTS

1. Cherry, J. T., N. Rimer, J. M. Savino and W. O. Wray [1975], "Improved Yield Determination and Event Identification Research," Systems, Science and Software Quarterly Technical Report, AFTAC/VSC, SSS-R-75-2696, August.

2. Savino, J. M., T. C. Bache, T. G. Barker, J. T. Cherry and W. O. Wray [1975], "Improved Yield Determination and Event Identification Research," Systems, Science and Software Quarterly Technical Report, AFTAC/VSC, SSS-R-76-2788, November.

3. Savino, J. M. [1976], "Improved Yield Determination and Event Identification Research," Systems, Science and Software Quarterly Technical Report, AFTAC/VSC, SSS-R-76-2870, February.

4. Bache, T. C., T. G. Barker, J. T. Cherry, N. Rimer and J. M. Savino [1976], "Explosion Source Modeling, Seismic Waveform Prediction and Yield Verification Research," Systems, Science and Software Quarterly Technical Report, AFTAC/VSC, SSS-R-76-2924, May.

5. Lambert, D. G., C. F. Petersen and J. M. Savino [1976], "Explosion Yield Verification, Multiple Explosion Scenarios and Three-Dimensional Seismic Modeling Research," Systems, Science and Software Quarterly Technical Report, AFTAC/VSC, SSS-R-76-2993, August.

B. TECHNICAL REPORTS

1. Cherry, J. T., N. Rimer and W. O. Wray [1975], "Seismic Coupling from a Nuclear Explosion: The Dependence of the Reduced Displacement Potential on the Nonlinear Behavior of the Near Source Rock Environment," Systems, Science and Software Technical Report, AFTAC/VSC, SSS-R-76-2742, September.

2. Garg, S. K. [1975], "Constitutive Equations for Fluid-Saturated Porous Media," Systems, Science and Software Topical Report, AFTAC/VSC, SSS-R-76-2766, October.

3. Cherry, J. T., T. C. Bache, W. O. Wray and J. F. Masso [1976], "Teleseismic Coupling from the Simultaneous Detonation of an Array of Nuclear Explosions," Systems, Science and Software Topical Report, AFTAC/VSC, SSS-R-76-2865, February.

4. Barker, T. G., T. C. Bache, J. T. Cherry, N. Rimer and J. M. Savino [1976], "Prediction and Matching of Tele-seismic Ground Motion (Body and Surface Waves) From the NTS MAST Explosion," Systems, Science and Software Topical Report, AFTAC/VSC, SSS-R-76-2727, February.

5. Bache, T. C., T. G. Barker, N. Rimer and J. M. Savino [1976], "Comparison of Theoretical and Observed Body and Surface Waves from KASSERI, and Explosion at NTS," Systems, Science and Software Topical Report, AFTAC/VSC, SSS-R-76-2937, May.

6. Bache, T. C. T. G. Barker, J. T. Cherry and J. M. Savino [1976], "Teleseismic Verification of Data Exchange Yields," Systems, Science and Software Topical Report, AFTAC/VSC, SSS-R-76-2941, May.